



TECH BRIEFS

NATIONAL AERONAUTICS AND SPACE ADMINISTRATION

-  **Technology Focus**
-  **Electronics/Computers**
-  **Software**
-  **Materials**
-  **Mechanics/Machinery**
-  **Manufacturing**
-  **Bio-Medical**
-  **Physical Sciences**
-  **Information Sciences**
-  **Books and Reports**

INTRODUCTION

Tech Briefs are short announcements of innovations originating from research and development activities of the National Aeronautics and Space Administration. They emphasize information considered likely to be transferable across industrial, regional, or disciplinary lines and are issued to encourage commercial application.

Availability of NASA Tech Briefs and TSPs

Requests for individual Tech Briefs or for Technical Support Packages (TSPs) announced herein should be addressed to

National Technology Transfer Center

Telephone No. (800) 678-6882 or via World Wide Web at www2.nttc.edu/leads/

Please reference the control numbers appearing at the end of each Tech Brief. Information on NASA's Innovative Partnerships Program (IPP), its documents, and services is also available at the same facility or on the World Wide Web at <http://ipp.nasa.gov>.

Innovative Partnerships Offices are located at NASA field centers to provide technology-transfer access to industrial users. Inquiries can be made by contacting NASA field centers listed below.

NASA Field Centers and Program Offices

Ames Research Center

Lisa L. Lockyer
(650) 604-1754
lisa.l.lockyer@nasa.gov

Dryden Flight Research Center

Gregory Poteat
(661) 276-3872
greg.poteat@dfrc.nasa.gov

Glenn Research Center

Kathy Needham
(216) 433-2802
kathleen.k.needham@nasa.gov

Goddard Space Flight Center

Nona Cheeks
(301) 286-5810
nona.k.cheeks@nasa.gov

Jet Propulsion Laboratory

Ken Wolfenbarger
(818) 354-3821
james.k.wolfenbarger@jpl.nasa.gov

Johnson Space Center

Michele Brekke
(281) 483-4614
michele.a.brekke@nasa.gov

Kennedy Space Center

David R. Makufka
(321) 867-6227
david.r.makufka@nasa.gov

Langley Research Center

Martin Waszak
(757) 864-4015
martin.r.waszak@nasa.gov

Marshall Space Flight Center

Jim Dowdy
(256) 544-7604
jim.dowdy@msfc.nasa.gov

Stennis Space Center

John Bailey
(228) 688-1660
john.w.bailey@nasa.gov

Carl Ray, Program Executive

Small Business Innovation
Research (SBIR) & Small
Business Technology
Transfer (STTR) Programs
(202) 358-4652
carl.g.ray@nasa.gov

Doug Comstock, Director

Innovative Partnerships
Program Office
(202) 358-2560
doug.comstock@nasa.gov



TECH BRIEFS

NATIONAL AERONAUTICS AND SPACE ADMINISTRATION



5 Technology Focus: Data Acquisition

- 5 WRATS Integrated Data Acquisition System
- 6 Breadboard Signal Processor for Arraying DSN Antennas
- 7 Digital Receiver Phase Meter
- 8 Split-Block Waveguide Polarization Twist for 220 to 325 GHz



9 Electronics/Computers

- 9 Nano-Multiplication-Region Avalanche Photodiodes and Arrays
- 10 Tailored Asymmetry for Enhanced Coupling to WGM Resonators
- 11 Disabling CNT Electronic Devices by Use of Electron Beams



13 Mechanics/Machinery

- 13 Conical Bearingless Motor/Generators
- 14 Integrated Force Method for Indeterminate Structures



17 Bio-Medical

- 17 Carbon-Nanotube-Based Electrodes for Biomedical Applications
- 18 Compact Directional Microwave Antenna for Localized Heating
- 19 Using Hyperspectral Imagery To Identify Turfgrass Stresses



21 Physical Sciences

- 21 Shaping Diffraction-Grating Grooves To Optimize Efficiency
- 22 Low-Light-Shift Cesium Fountain Without Mechanical Shutters
- 23 Magnetic Compensation for Second-Order Doppler Shift in LITS

- 24 Nanostructures Exploit Hybrid-Polariton Resonances
- 25 Microfluidics, Chromatography, and Atomic-Force Microscopy
- 26 Model of Image Artifacts From Dust Particles



29 Information Sciences

- 29 Pattern-Recognition System for Approaching a Known Target
- 30 Orchestrator Telemetry Processing Pipeline
- 30 Scheme for Quantum Computing Immune to Decoherence



31 Books & Reports

- 31 Spin-Stabilized Microsatellites With Solar Concentrators
- 31 Phase Calibration of Antenna Arrays Aimed at Spacecraft
- 31 Ring Bus Architecture for a Solid-State Recorder
- 31 Image Compression Algorithm Altered To Improve Stereo Ranging

This document was prepared under the sponsorship of the National Aeronautics and Space Administration. Neither the United States Government nor any person acting on behalf of the United States Government assumes any liability resulting from the use of the information contained in this document, or warrants that such use will be free from privately owned rights.



Technology Focus: Data Acquisition

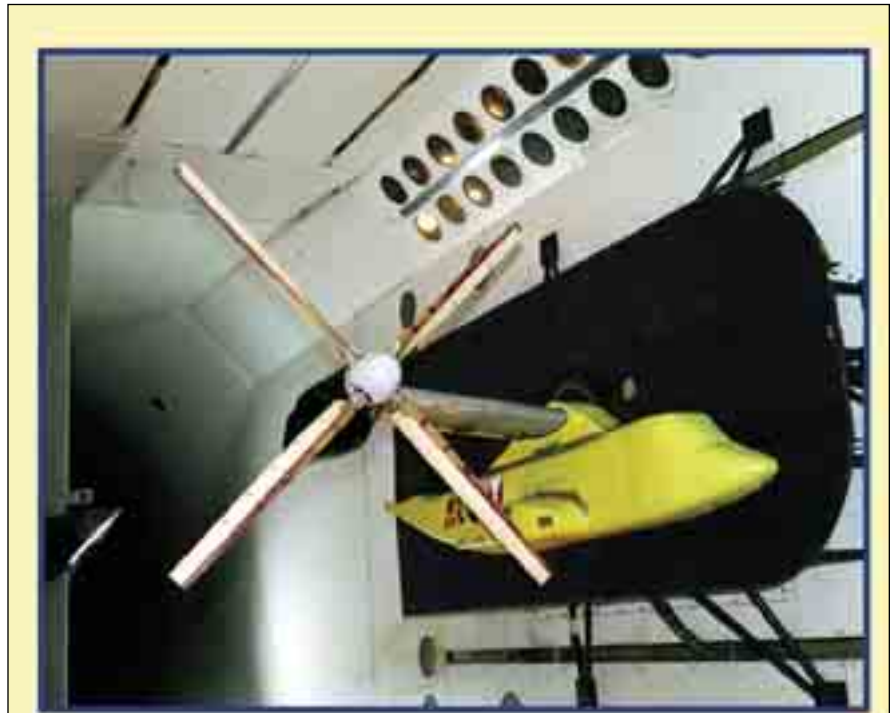
WRATS Integrated Data Acquisition System

This new system substantially improves tiltrotor aeroelastic test methods.

NASA Langley Research Center, Hampton, Virginia

The Wing and Rotor Aeroelastic Test System (WRATS) data acquisition system (DAS) is a 64-channel data acquisition display and analysis system specifically designed for use with the WRATS 1/5-scale V-22 tiltrotor model of the Bell Osprey. It is the primary data acquisition system for experimental aeroelastic testing of the WRATS model for the purpose of characterizing the aeromechanical and aeroelastic stability of prototype tiltrotor configurations. The WRATS DAS was also used during aeroelastic testing of Bell Helicopter Textron's Quad-Tiltrotor (QTR) design concept, a test which received international attention. The LabVIEW-based design is portable and capable of powering and conditioning over 64 channels of dynamic data at sampling rates up to 1,000 Hz. The system includes a 60-second circular data archive, an integrated model swashplate excitation system, a moving block damping application for calculation of whirl flutter mode subcritical damping, a loads and safety monitor, a pilot-control console display, data analysis capabilities, and instrumentation calibration functions. Three networked computers running custom-designed LabVIEW software acquire data through National Instruments data acquisition hardware.

The aeroelastic model (see figure) was tested with the DAS at two facilities at NASA Langley, the Transonic Dynamics Tunnel (TDT) and the Rotorcraft Hover Test Facility (RHTF). Because of the need for seamless transition between testing at these facilities, DAS is portable. The software is capable of harmonic analysis of periodic time history data, Fast Fourier Transform calculations, power spectral density calculations, and on-line calibration of test instrumentation. DAS has a circular buffer archive to ensure critical data is not lost in event of model failure/incident, as well as a sample-and-hold capability for phase-correct time history data. The system has an interface to drive TDT text overlay display video monitors and an interface to trigger digital video recording



Wing and Rotor Aeroelastic Test System 9 (WRATS).



WRATS DAS front panel graphical user interface.

The WRATS model was tested with the DAS at the Transonic Dynamics Tunnel at NASA Langley. Shown below is the LabVIEW-based WRATS DAS front-panel graphical user interface.

(DVR) systems.

DAS uses NI SCXI signal-conditioning hardware to power, amplify, and anti-alias-filter the 64 channels of sample-and-hold time-correlated data at sample rates up to 1,000 Hz. The WRATS data system as a whole maximizes efficient tiltrotor aeroelastic test practices at the TDT by allowing seamless integration of model swashplate stik-stir excitation commands with data

acquisition capabilities and post-point damping analysis. Following analysis, the system reports key results to a MATLAB-based data logging system for archiving, organization, and reporting of test results.

In addition to test efficiency, the system improves the safety-of-flight environment of the test process by calculating and monitoring critical model loads, stress, and parameters in real

time during testing. In the event of unsafe conditions or loads, audible, synthesized voice alerts are provided to the test crew in addition to visual display cues on the WRATS Loads Monitor displays, which are networked with the WRATS data system.

This work was done by David J. Piatak of Langley Research Center. Further information is contained in a TSP (see page 1). LAR-17486

Breadboard Signal Processor for Arraying DSN Antennas

The processors can be used to combine signals in interferometry and telecommunications.

NASA's Jet Propulsion Laboratory, Pasadena, California

A recently developed breadboard version of an advanced signal processor for arraying many antennas in NASA's Deep Space Network (DSN) can accept inputs in a 500-MHz-wide frequency band from six antennas. The next breadboard version is expected to accept inputs from 16 antennas, and a following developed version is expected to be designed according to an architecture that will be scalable to accept inputs from as many as 400 antennas. These and similar signal processors could also be used for combining multiple wide-band signals in non-DSN applications, including very-long-baseline interferometry and telecommunications.

This signal processor performs functions of a wide-band FX correlator and a beam-forming signal combiner. [The term "FX" signifies that the digital samples of two given signals are fast Fourier transformed (F), then the fast Fourier transforms of the two signals are multiplied (X) prior to accumulation.] In this processor, the signals from the various antennas are broken up into channels in the frequency domain (see figure). In each frequency channel, the

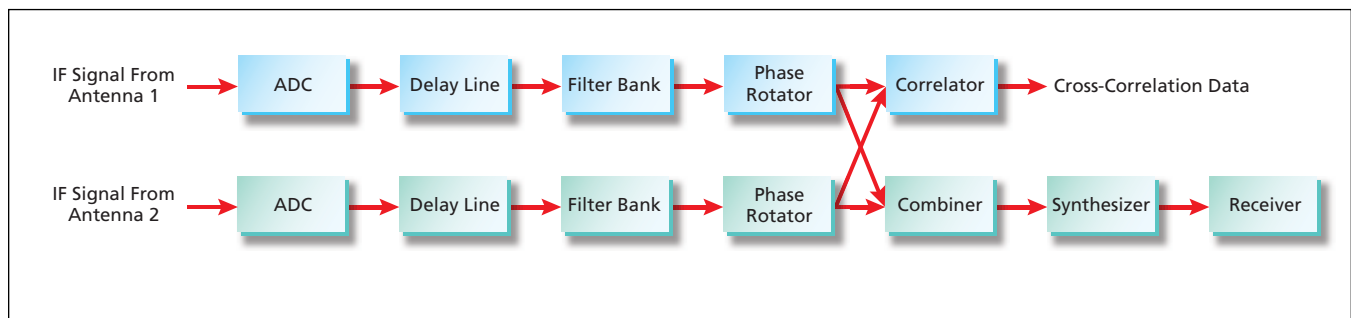
data from each antenna are correlated against the data from each other antenna; this is done for all antenna baselines (that is, for all antenna pairs). The results of the correlations are used to obtain calibration data to align the antenna signals in both phase and delay. Data from the various antenna frequency channels are also combined and calibration corrections are applied. The frequency-domain data thus combined are then synthesized back to the time domain for passing on to a telemetry receiver.

The inputs from the antennas are preprocessed signals in an intermediate-frequency (IF) band from 700 to 1,200 MHz. High-speed commercial off-the-shelf analog-to-digital-converter (ADC) integrated circuits sample the inputs to 8 bits at a rate of 1,280 MHz. The sample data are transmitted via fiber-optic links to signal-processing boards in a commercial high-performance, modular, digital chassis that conforms to an industry standard known as the Advanced Telecommunications Architecture (ATCA). The physical and electrical characteristics of an ATCA chassis are governed by a specification known

as PICMG 3.0 (wherein "PICMG" signifies the PCI Industrial Computer Manufacturers Group and "PCI" signifies peripheral component interface).

Mounted on each signal-processing board are four field-programmable gate array (FPGA) integrated-circuit chips that are interconnected both on the board and through the ATCA back plane by serial links capable of operating at speeds up to 2.5 Gb/s. Each FPGA chip can be programmed, independently of the other FPGA chips, to perform such specific functions as implementing filter banks to convert time-domain data to frequency-domain data in frequency channels, wide- and narrow-band cross-correlation, combining of the individual frequency channels, and implementing synthesizing filter banks for converting frequency-domain data back to the time domain.

This work was done by Andre Jongeling, Elliott Sigman, Kumar Chandra, Joseph Trinh, Melissa Soriano, Robert Navarro, Stephen Rogstad, Charles Goodhart, Robert Proctor, Michael Jourdan, and Benno Rayhrer of Caltech for NASA's Jet Propulsion Laboratory. Further information is contained in a TSP (see page 1). NPO-43646



This **Block Diagram** is a simplified representation the signal flow downstream of the inputs from two antennas. Each filter bank converts time-domain data to frequency-domain data in 400 overlapping 1.25-MHz-wide frequency channels that span the IF range from 700 to 1,200 MHz. The combiner, synthesizer, and receiver were undergoing development at the time of reporting the information for this article.

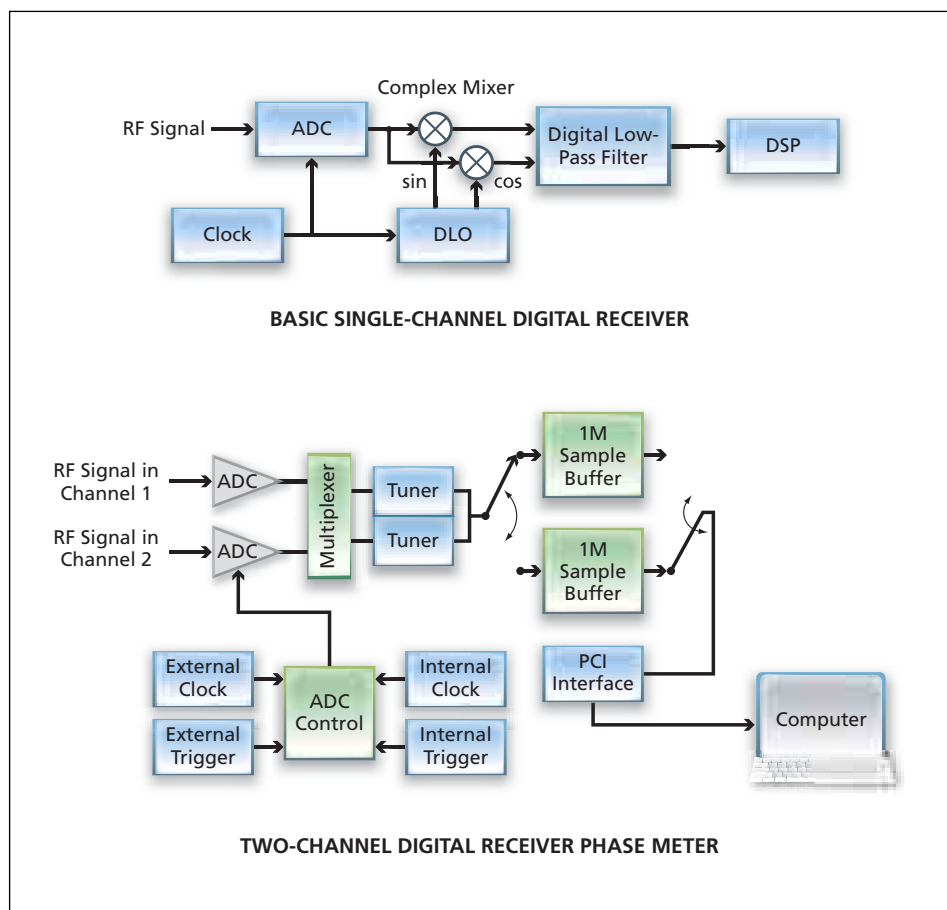
Digital Receiver Phase Meter

A commercial digital receiver is modified into a two-channel phase meter.

NASA's Jet Propulsion Laboratory, Pasadena, California

The software of a commercially available digital radio receiver has been modified to make the receiver function as a two-channel low-noise phase meter. This phase meter is a prototype in the continuing development of a phase meter for a system in which radio-frequency (RF) signals in the two channels would be outputs of a spaceborne heterodyne laser interferometer for detecting gravitational waves. The frequencies of the signals could include a common Doppler-shift component of as much as 15 MHz. The phase meter is required to measure the relative phases of the signals in the two channels at a sampling rate of 10 Hz at a root power spectral density $<5 \text{ microcycle}/(\text{Hz})^{1/2}$ and to be capable of determining the power spectral density of the phase difference over the frequency range from 1 mHz to 1 Hz. Such a phase meter could also be used on Earth to perform similar measurements in laser metrology of moving bodies.

To illustrate part of the principle of operation of the phase meter, the figure includes a simplified block diagram of a basic single-channel digital receiver. The input RF signal is first fed to the input terminal of an analog-to-digital converter (ADC). To prevent aliasing errors in the ADC, the sampling rate must be at least twice the input signal frequency. The sampling rate of the ADC is governed by a sampling clock, which also drives a digital local oscillator (DLO), which is a direct digital frequency synthesizer. The DLO produces samples of sine and cosine signals at a programmed tuning frequency. The sine and cosine samples are mixed with (that is, multiplied by) the samples from the ADC, then low-pass filtered to obtain in-phase (I) and quadrature (Q) signal components. A digital signal processor (DSP) computes the ratio between the Q and I components, computes the phase of the RF signal (relative to that of the DLO signal) as the arctangent of this ratio, and then averages successive such phase values over a time interval specified by the user.



These Block Diagrams depict the principles of operation of (1) a basic single-channel digital receiver and (2) the present two-channel digital phase meter, which utilizes the original hardware and modified software of a commercial two-channel digital receiver.

The specific commercially available two-channel digital receiver includes a dual-channel, 65-MHz, 14-bit peripheral component interface (PCI) bus data-acquisition card with a daughter board that contains a pair of narrow-band tuner integrated-circuit chips. The input stage of the card consists of two ADCs. In the tuner chips, input signals having frequencies up to 35 MHz can be translated to zero frequency, then digitally low-pass filtered to a bandwidth between 1 kHz and 1 MHz. The output samples of the tuner chips are fed to a two-part swap buffer. When each half of the swap buffer becomes filled up to a limit (e.g., 1M sample) specified by the user, the contents of the buffer are transferred, via PCI interface, to an external computer for further analysis.

The factory-supplied receiver software includes basic driver components

and provides many options to control tuning frequencies, sampling rates, and other operational parameters. The phase-meter version of the software incorporates many of the basic driver components, but a significant effort was made in modifying other parts of the software to make the receiver function as a dedicated two-channel phase meter. In essence, the net effect of the modification is to cause the external computer to calculate differences between the phases in each successive pair of buffered samples from tuner chips and calculate the average phase difference over the time interval represented by the buffer contents.

This work was done by Martin Marcin and Alexander Abramovici of Caltech for NASA's Jet Propulsion Laboratory. For more information, contact iaoffice@jpl.nasa.gov. NPO-43928

Split-Block Waveguide Polarization Twist for 220 to 325 GHz

This device is superior to conventional twisted rectangular waveguides for submillimeter wavelengths.

NASA's Jet Propulsion Laboratory, Pasadena, California

A split-block waveguide circuit that rotates polarization by 90° has been designed with WR-3 input and output waveguides, which are rectangular waveguides used for a nominal frequency range of 220 to 325 GHz. Heretofore, twisted rectangular waveguides equipped with flanges at the input and output have been the standard means of rotating the polarizations of guided microwave signals. However, the fabrication and assembly of

such components become difficult at high frequency due to decreasing wavelength, such that twisted rectangular waveguides become impractical at frequencies above a few hundred gigahertz. Conventional twisted rectangular waveguides are also not amenable to integration into highly miniaturized subassemblies of advanced millimeter- and submillimeter-wave detector arrays now undergoing development. In contrast,

the present polarization-rotating waveguide can readily be incorporated into complex integrated waveguide circuits such as miniaturized detector arrays fabricated by either conventional end milling of metal blocks or by deep reactive ion etching of silicon blocks. Moreover, the present split-block design can be scaled up in frequency to at least 5 THz. The main step in fabricating a split-

block polarization-rotating waveguide of the present design is to cut channels having special asymmetrically shaped steps into mating upper and lower blocks (see Figure 1). The dimensions of the steps are chosen to be consistent with the WR-3 waveguide cross section, which is 0.864 by 0.432 mm. The channels are characterized by varying widths with constant depths of 0.432, 0.324, and 0.216 mm and by relatively large corner radii to facilitate fabrication. The steps effect both a geometric transition and the corresponding impedance-matched electromagnetic-polarization transition between (1) a WR-3 rectangular waveguide oriented with the electric field vector normal to the block mating surfaces and (2) a corresponding WR-3 waveguide oriented with its electric field vector parallel to the mating surfaces of the blocks.

A prototype has been built and tested. Figure 2 presents test results indicative of good performance over nearly the entire WR-3 waveguide frequency band. This work was done by John Ward and Goutam Chattopadhyay of Caltech for NASA's Jet Propulsion Laboratory. Further information is contained in a TSP (see page 1). NPO-42985

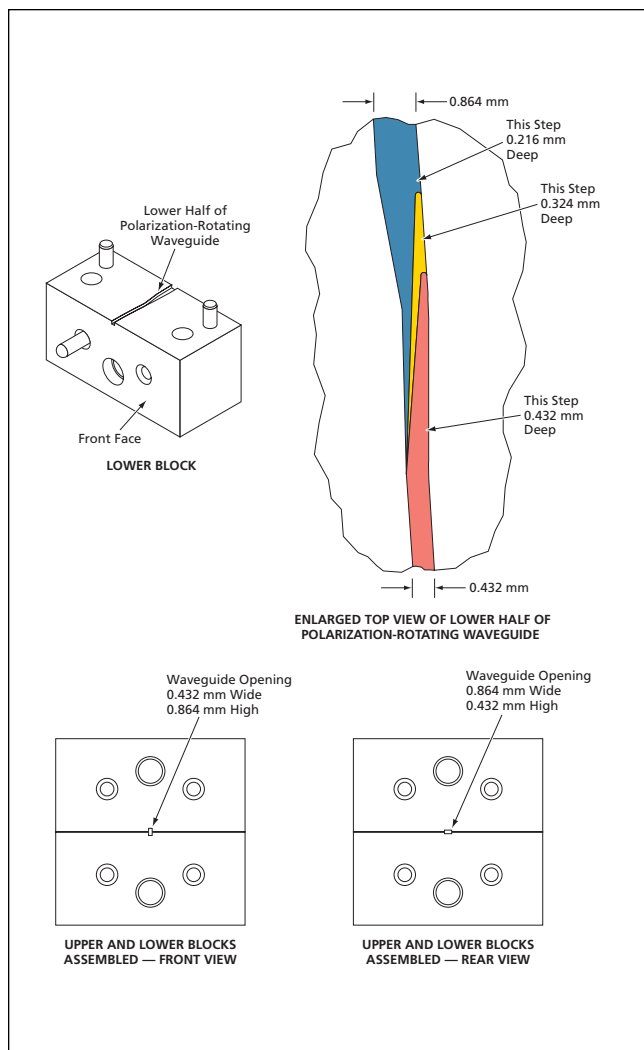


Figure 1. A Channel Having Asymmetric Steps is cut into the lower block. An identical channel is cut into the upper block. Then with the help of alignment pins, the blocks are assembled so that the two channels merge into one channel that makes a transition between two orthogonal orientations of a WR-3 waveguide.

block polarization-rotating waveguide of the present design is to cut channels having special asymmetrically shaped steps into mating upper and lower blocks (see Figure 1). The dimensions of the steps are chosen to be consistent with the WR-3 waveguide cross section, which is 0.864 by 0.432 mm. The channels are characterized by varying widths with constant depths of 0.432, 0.324, and 0.216 mm and by relatively large corner radii to facilitate fabrication. The steps effect both a geometric transition and the corresponding impedance-matched electromagnetic-polarization transition between (1) a WR-3 rectangular waveguide oriented with the electric field vector normal to the block mating surfaces and (2) a corresponding WR-3 waveguide oriented with its electric field vector parallel to the mating surfaces of the blocks.

A prototype has been built and tested. Figure 2 presents test results indicative of good performance over nearly the entire WR-3 waveguide frequency band. Moreover, the present split-block design can be scaled up in frequency to at least 5 THz. The main step in fabricating a split-

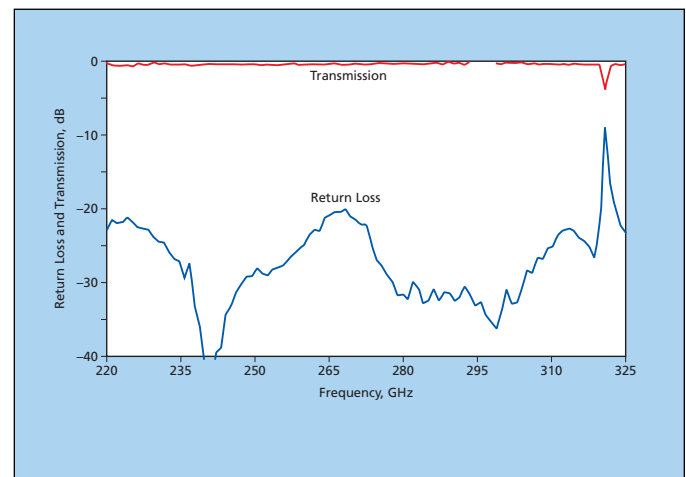


Figure 2. The Return Loss and Transmission of a prototype of a polarization-rotating waveguide like that of Figure 1 was measured over the nominal frequency band of WR-3 waveguide.



Nano-Multiplication-Region Avalanche Photodiodes and Arrays

Oxide embedding structures and nanoscale multiplication regions would afford improvements in performance.

NASA's Jet Propulsion Laboratory, Pasadena, California

Nano-multiplication-region avalanche photodiodes (NAPDs), and imaging arrays of NAPDs integrated with complementary metal oxide/semiconductor (CMOS) active-pixel-sensor integrated circuitry, are being developed for applications in which there are requirements for high-sensitivity (including photon-counting) detection and imaging at wavelengths from about 250 to 950 nm. With respect to sensitivity and to such other characteristics as speed, geometric array format, radiation hardness, power demand of associated circuitry, size, weight, and robustness, NAPDs and ar-

rays thereof are expected to be superior to prior photodetectors and arrays including CMOS active-pixel sensors (APSs), charge-coupled devices (CCDs), traditional APDs, and microchannel-plate/CCD combinations.

Figure 1 depicts a conceptual NAPD array, integrated with APS circuitry, fabricated on a thick silicon-on-insulator wafer (SOI). Figure 2 presents selected aspects of the structure of a typical single pixel, which would include a metal oxide/semiconductor field-effect transistor (MOSFET) integrated with the NAPD. The NAPDs would reside in sili-

con islands formed on the buried oxide (BOX) layer of the SOI wafer. The silicon islands would be surrounded by oxide-filled insulation trenches, which, together with the BOX layer, would constitute an oxide embedding structure. There would be two kinds of silicon islands: NAPD islands for the NAPDs and MOSFET islands for in-pixel and global CMOS circuits. Typically, the silicon islands would be made between 5 and 10 μm thick, but, if necessary, the thickness could be chosen outside this range. The side walls of the silicon islands would be heavily doped with electron-acceptor impurities (p^+ -doped) to form anodes for the photodiodes and guard layers for the MOSFETs.

A nanoscale reach-through structure at the front (top in the figures) central position of each NAPD island would contain the APD multiplication region. Typically, the reach-through structure would be about 0.1 μm in diameter and between 0.3 and 0.4 nm high. The top layer in the reach-through structure would be heavily doped with electron-donor impurities (n^+ -doped) to make it act as a cathode. A layer beneath the cathode, between 0.1 and 0.2 nm thick, would be p -doped to a concentration $\approx 10^{17} \text{ cm}^{-3}$. A thin n^+ -doped polysilicon pad would be formed on the top of the cathode to protect the cathode against erosion during a metal-silicon alloying step that would be part of the process of fabricating the array. This NAPD structure would be amenable to either front or back illumination. To enable back illumination, it would be necessary to etch away, from underneath the NAPD silicon islands, the corresponding portions of a handle wafer supporting the SOI substrate.

The advantages of the NAPD concept over prior photodetector and array concepts are attributable to the oxide embedding SOI structure and the nanoscale multiplication region. The electrically insulating property of the oxide embedding structure would prevent cross-talk among pixels. The

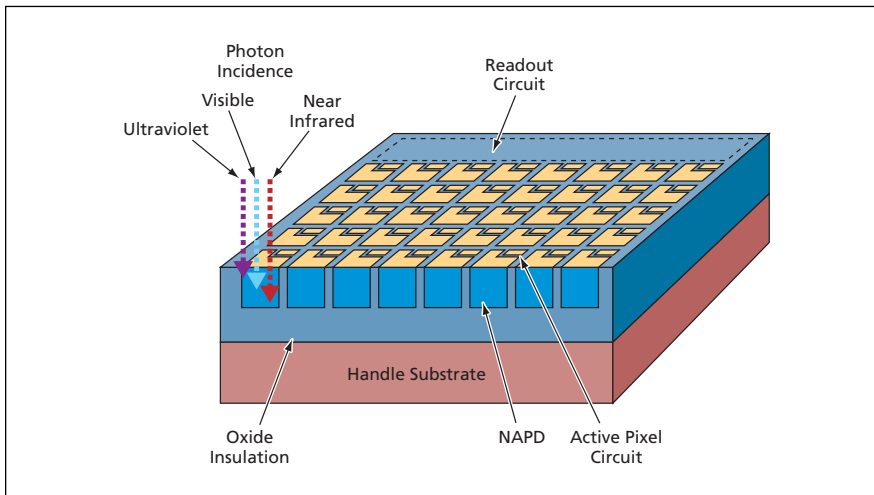


Figure 1. A typical NAPD array, characterized by a high fill factor, would be integrated with active pixel circuits and an on-chip readout circuit.

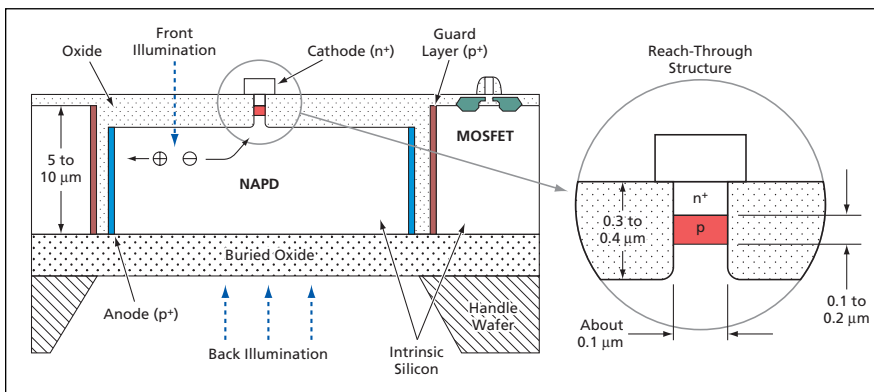


Figure 2. Each pixel of an array like that of Figure 1 would contain a NAPD structure integrated with an active pixel circuit structure that, in this example, would be a MOSFET structure.

nanoscale design of the multiplication region could be tailored to obtain unique avalanche properties. In contrast, (1) the pixels of a traditional APD array are all built on one common substrate, leading to severe cross-talk and (2) a traditional APD contains a relatively large multiplication region, within which electron avalanches are localized to a few small volumes. Efforts have been made to obtain uniformity in the multiplication regions of traditional APDs,

but inasmuch as electron avalanches are very sensitive to the local electric-field fluctuations, it is difficult to obtain uniformity in large arrays of conventional APDs.

This work was done by Xinyu Zheng, Bedabrata Pain, and Thomas Cunningham of Caltech for NASA's Jet Propulsion Laboratory. Further information is contained in a TSP (see page 1).

In accordance with Public Law 96-517, the contractor has elected to retain title to this

invention. Inquiries concerning rights for its commercial use should be addressed to:

*Innovative Technology Assets Management
JPL*

*Mail Stop 202-233
4800 Oak Grove Drive
Pasadena, CA 91109-8099
(818) 354-2240*

E-mail: iaoffice@jpl.nasa.gov

Refer to NPO-42276, volume and number of this NASA Tech Briefs issue, and the page number.

Tailored Asymmetry for Enhanced Coupling to WGM Resonators

Surfaces are made to have optimum combinations of curvatures in orthogonal planes.

NASA's Jet Propulsion Laboratory, Pasadena, California

Coupling of light into and out of whispering-gallery-mode (WGM) optical resonators can be enhanced by designing and fabricating the resonators to have certain non-axisymmetric shapes (see figure). Such WGM resonators also exhibit the same ultrahigh values of the resonance quality factor (Q) as do prior WGM resonators. These WGM resonators are potentially useful as tunable narrow-band optical filters having throughput levels near unity, high-speed optical switches, and low-threshold laser resonators. These WGM resonators could also be used in experiments to investigate coupling between high- Q and chaotic modes within the resonators.

For a WGM resonator made of an optically nonlinear material (e.g., lithium niobate) or another material having a high index of refraction, a prism made of a material having a higher index of refraction (e.g., diamond) must be used as part of the coupling optics. For coupling of a beam of light into (or out of) the high- Q resonator modes, the beam must be made to approach (or recede from) the resonator at a critical angle determined by the indices of refraction of the resonator and prism materials. In the case of a lithium niobate/diamond interface, this angle is approximately 22° .

For a beam of laser light traveling through the prism and having a typical axisymmetric cross-sectional power density that varies as a Gaussian function of radius from its cylindrical axis, the cross section of the phase front changes from circular to elliptical at the interface. In the case of the lithium niobate/diamond interface, the ratio between the lengths of the semimajor and semiminor axes of the ellipse is about 2.7. In order

to optimize the coupling of the beam into the high- Q modes of the resonator, the ratio between the horizontal and vertical curvatures of the resonator must be made to equal the aforesaid material-dependent ratio between the lengths of the axes of the ellipse. (Here, "vertical" and "horizontal" refer to planes onto which are projected the narrowest and widest views, respectively, of the resonator, as in the figure.) It is difficult to fabricate a WGM resonator surface to such an exacting specification at a specific point on its surface, but the task can be simplified as described next if one does not insist on a specific location.

If the WGM resonator is shaped to have a constant radius of curvature at its periphery as seen in a vertical plane but is asymmetrical (or at least non-axisymmetric) in a horizontal plane (for example, if its shape in a horizontal plane is elliptical), then its horizontal radius of curvature and the ratio between the two curvatures varies continuously with position along the periphery. Consequently, by suitable choice of the shape, it is possible to make the ratio between these curvatures equal the desired material-dependent ratio at some location along the periphery.

Several working prototype WGM resonators have been designed and fabricated according to this concept. In tests, these resonators exhibited Q values of about 10^8 and coupling efficiencies >0.7 .

This work was done by Makan Mohageg and Lute Maleki of Caltech for NASA's Jet Propulsion Laboratory. Further information is contained in a TSP (see page 1).

In accordance with Public Law 96-517, the contractor has elected to retain title to this invention. Inquiries concerning rights for its commercial use should be addressed to:



In the **Non-Axisymmetric Resonator**, the variation of curvature along the periphery in the horizontal plane is chosen such that the ratio between the horizontal and vertical curvatures has the optimum value at some location.

*Innovative Technology Assets Management
JPL*

*Mail Stop 202-233
4800 Oak Grove Drive
Pasadena, CA 91109-8099
(818) 354-2240*

E-mail: iaoffice@jpl.nasa.gov

Refer to NPO-43832, volume and number of this NASA Tech Briefs issue, and the page number.

Disabling CNT Electronic Devices by Use of Electron Beams

Selected CNTs would be burned out.

NASA's Jet Propulsion Laboratory, Pasadena, California

Bombardment with tightly focused electron beams has been suggested as a means of electrically disabling selected individual carbon-nanotubes (CNTs) in electronic devices. Evidence in support of the suggestion was obtained in an experiment in which a CNT field-effect transistor was disabled (see figure) by focusing a 1-keV electron beam on a CNT that served as the active channel of a field-effect transistor (FET).

Such bombardment could be useful in the manufacture of nonvolatile-mem-

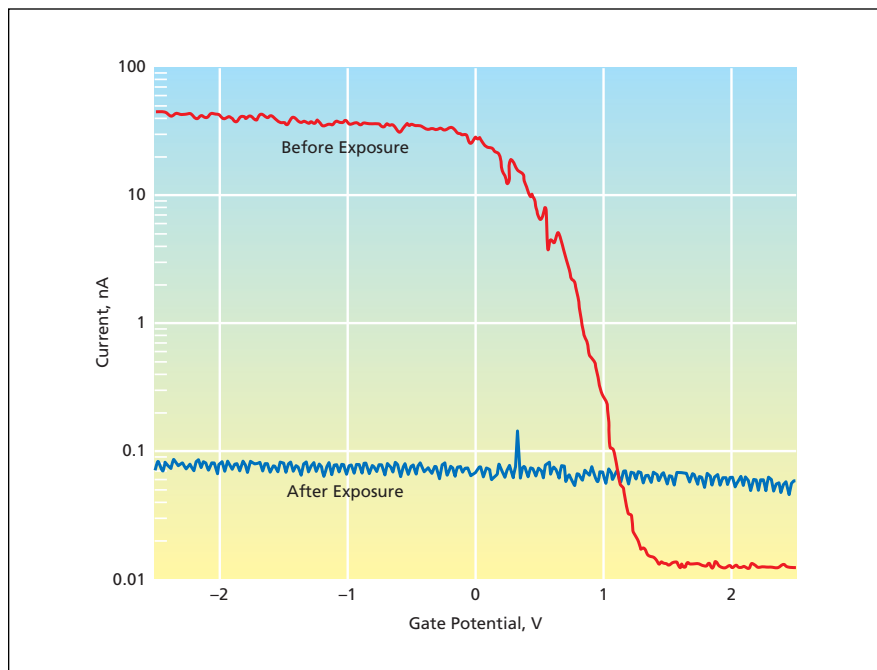
ory circuits containing CNT FETs. Ultimately, in order to obtain the best electronic performances in CNT FETs and other electronic devices, it will be necessary to fabricate the devices such that each one contains only a single CNT as an active element. At present, this is difficult because there is no way to grow a single CNT at a specific location and with a specific orientation. Instead, the common practice is to build CNTs into electronic devices by relying on spatial distribution to bridge contacts. This

practice results in some devices containing no CNTs and some devices containing more than one CNT. Thus, CNT FETs have statistically distributed electronic characteristics (including switching voltages, gains, and mixtures of metallic and semiconducting CNTs).

According to the suggestion, by using a 1-keV electron beam (e.g., a beam from a scanning electron microscope), a particular nanotube could be rendered electrically dysfunctional. This procedure could be repeated as many times as necessary on different CNTs in a device until all of the excess CNTs in the device had been disabled, leaving only one CNT as an active element (e.g., as FET channel).

The physical mechanism through which a CNT becomes electrically disabled is not yet understood. On one hand, data in the literature show that electron kinetic energy >86 keV is needed to cause displacement damage in a CNT. On the other hand, inasmuch as a 1-keV beam focused on a small spot (typically a few tens of nanometers wide) deposits a significant amount of energy in a small volume, the energy density may suffice to thermally induce structural and/or electronic changes that disable the CNT. Research may be warranted to investigate this effect in detail.

*This work was done by Mihail Petkov of Caltech for NASA's Jet Propulsion Laboratory. Further information is contained in a TSP (see page 1).
NPO-41343*



The Functionality of a CNT FET was destroyed by exposure to a focused 1-keV electron beam.



Conical Bearingless Motor/Generators

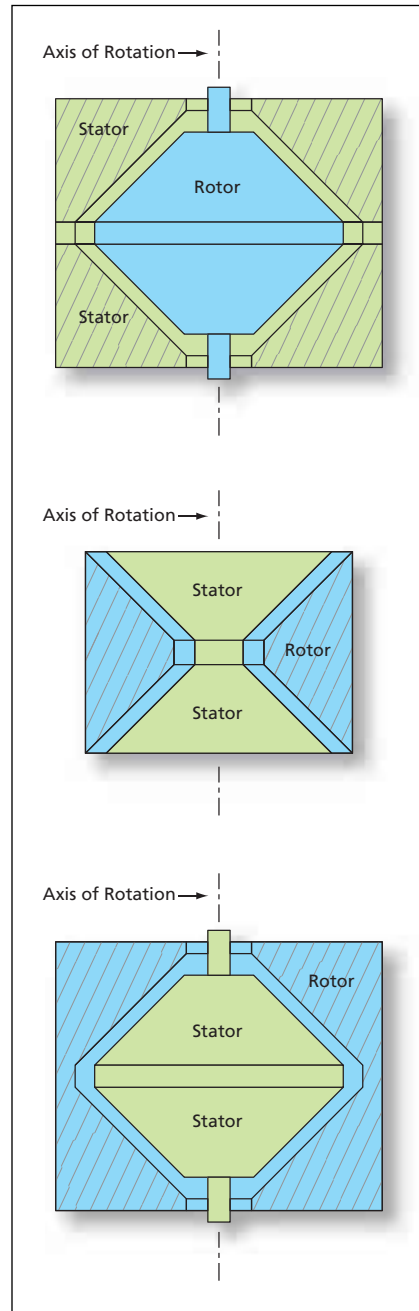
Advantages include high-speed, long-life operation in a compact form factor.

John H. Glenn Research Center, Cleveland, Ohio

Motor/generators based on conical magnetic bearings have been invented as an improved alternative to prior such machines based, variously, on radial and/or axial magnetic bearings. Both the present and prior machines are members of the class of so-called “bearingless” or “self bearing” (in the sense of not containing mechanical bearings) rotary machines. Each motor/generator provides both a torque and force allowing it to either function as a motor and magnetic bearing or a generator and magnetic bearing concurrently. Because they are not subject to mechanical bearing wear, these machines have potentially long operational lives and can function without lubrication and over wide ranges of speed and temperature that include conditions under which lubricants would become depleted, degraded, or ineffective and mechanical bearings would fail.

The figure shows three typical configurations of conical bearingless motor/generators. The main elements of each motor/generator are concentric rotor and stator portions having conically tapered surfaces facing each other across a gap. Because a conical motor/generator imposes both radial and axial magnetic forces, it acts, in effect, as a combination of an axial and a radial magnetic bearing. Therefore, only two conical motor/generators — one at each end of a rotor — are needed to effect complete magnetic levitation of the rotor, whereas previously, it was necessary to use a combination of an axial and a radial magnetic bearing at each end of the rotor to achieve complete magnetic levitation and a separate motor to provide torque.

The stator portion of each motor/generator consists of a magnetic core and back iron with a number of teeth and slots at the gap and wires (electromagnet coils) wound in the slots. The rotor consists largely of a magnetic core and, depending on the specific design, could also include permanent magnets. Except for the conical



Conical Bearingless Motor/Generators both levitate and rotate the rotor with respect to the stators. These are simplified cross-sectional views of representative configurations of machines described in the text. Although stators traditionally enclose rotors, conical bearingless motor/generators lend themselves equally well to designs in which rotors enclose stators.

configuration, the rotor and stator resemble those of prior radial magnetic bearings and bearingless motors.

As in prior magnetic bearings and bearingless motors, electric currents are driven through the coils, producing magnetic fluxes in the core and rotor that result in torques and forces on the rotor; a feedback control system adjusts the current waveforms, in response to the positions of the ends of the rotor as measured by sensors, to produce the radial and axial forces needed to maintain rotor levitation at the desired radial and axial position. For motor or generator operation, times for electronic switching of coil connections for input or output currents are determined in response to the rotation angle as measured by another sensor.

Unlike in prior bearingless motors, it is not necessary to use one set of coils for levitation interspersed with another sets of coils for motor/generator operation. Instead, an improved control scheme provides for the use of a single set of coils for both levitation and motor/generator operation. The scheme requires at least six coils (for three or more pole pairs) in each bearing. In its motor aspect, the scheme provides for simultaneous operation of the equivalent of three overlapping three-phase motors. In addition, this motor configuration provides a certain amount of fault tolerance; if any of the pole-pair coils or the drive circuitry of a pole pair fails, the remaining two three-phase subsystems can continue to provide magnetic levitation and motor/generator operation.

This work was done by P. Kascah and R. Jansen of the University of Toledo and T. Dever of QSS Group, Inc. for Glenn Research Center. Further information is contained in a TSP (see page 1).

Inquiries concerning rights for the commercial use of this invention should be addressed to NASA Glenn Research Center, Innovative Partnerships Office, Attn: Steve Fedor, Mail Stop 4-8, 21000 Brookpark Road, Cleveland, Ohio 44135. Refer to LEW-17638-1/39-1/40-1.

⚙️ Integrated Force Method for Indeterminate Structures

Indeterminate structural-mechanics problems can now be solved systematically.

John H. Glenn Research Center, Cleveland, Ohio

Two methods of solving indeterminate structural-mechanics problems have been developed as products of research on the theory of strain compatibility. In these methods, stresses are considered to be the primary unknowns (in contrast to strains and displacements being considered as the primary unknowns in some prior methods). One of these methods, denoted the integrated force method (IFM), makes it possible to compute stresses, strains, and displacements with high fidelity by use of modest finite-element models that entail relatively small amounts of computation. The other method, denoted the completed Beltrami Mitchell formulation (CBMF), enables direct determination of stresses in an elastic continuum with general boundary conditions, without the need to first calculate displacements as in traditional methods.

The equilibrium equation, the compatibility condition, and the material law are the three fundamental concepts of the theory of structures. For almost 150 years, it has been commonly supposed that the theory is complete. However, until now, the understanding of the compatibility condition remained

incomplete, and the compatibility condition was confused with the continuity condition. Furthermore, the compatibility condition as applied to structures in its previous incomplete form was inconsistent with the strain formulation in elasticity.

Strength-of-materials problems have been classified into determinate and indeterminate problems. A determinate problem is analyzed primarily on the basis of the equilibrium concept and can be well understood. The solution of an indeterminate problem requires an additional compatibility condition, of which, until now, there has not been exclusive comprehension. In traditional stress-analysis methods, the compatibility condition has been improvised by manipulating the equilibrium concept, variously, by rewriting it in displacement variables or through a method known in the art as the redundant force method. Such improvisation has made traditional indeterminate analysis cumbersome.

The research that led to the development of the IMF and the CBMF included the derivation of a variational functional. The stationary condition of this functional yielded not only the tra-

ditional equations of the mechanics of solids but also new equations that were identified as constituting the boundary compatibility condition that was missing from the strain equations as originally formulated by St. Venant circa 1860. It should be noted that the IFM and the CBMF can be further specialized into four indirect methods known as the redundant force method, stiffness method, the hybrid method, and the total formulation (see table)

The use of the compatibility equations has systematized indeterminate analysis — especially for problems that involve variations in temperature and initial deformations. Solving indeterminate problems has become straightforward through use of the IFM because the IFM bestows simultaneous emphasis on force equilibrium and the deformation compatibility condition.

A report, “Integrated Force Method Solution to Indeterminate Structural Mechanics Problems” (NASA/TP-2004-207430) introduces the IFM to academia, especially to engineering students in civil, mechanical, aeronautical, and other engineering disciplines. Although the report is written for use in college education, it should be valuable to researchers who

Method		Primary Variables		Variational Functional
Elasticity	Structures	Elasticity	Structures	
Completed Beltrami-Michell Formulation (CBMF)	Integrated Force Method (IFM)	Stresses	Forces	IFM Variational Functional
Airy Formulation	Redundant Force Method	Stress Function	Redundants	Complementary Energy
Navier Formulation (NF)	Stiffness Method (DM)	Displacements	Displacements or Deflections	Potential Energy
Reissner Method (RM)	Hybrid Method (HF)	Stresses and Displacements	Forces and Deflections	Reissner Functional
Total Formulation (TF)	Washizu Method (WM)	Stresses, Strains, and Displacements	Forces, Deformations, and Deflections	Washizu Functional

Selected Characteristics of the IFM and CBMF are listed along with those of other methods of structural mechanics.

wish to work on the IFM or to complement their understanding of the compatibility condition of structural mechanics.

This work was done by Dale A. Hopkins and Gary R. Halford of Glenn Research Cen-

ter and Surya N. Patnaik of Ohio Aerospace Institute. Further information is contained in a TSP (see page 1).

Inquiries concerning rights for the commercial use of this invention should be ad-

dressed to NASA Glenn Research Center, Innovative Partnerships Office, Attn: Steve Fedor, Mail Stop 4-8, 21000 Brookpark Road, Cleveland, Ohio 44135. Refer to LEW-17883-1.



Carbon-Nanotube-Based Electrodes for Biomedical Applications

Stimuli and responses could be localized to within nanometers.

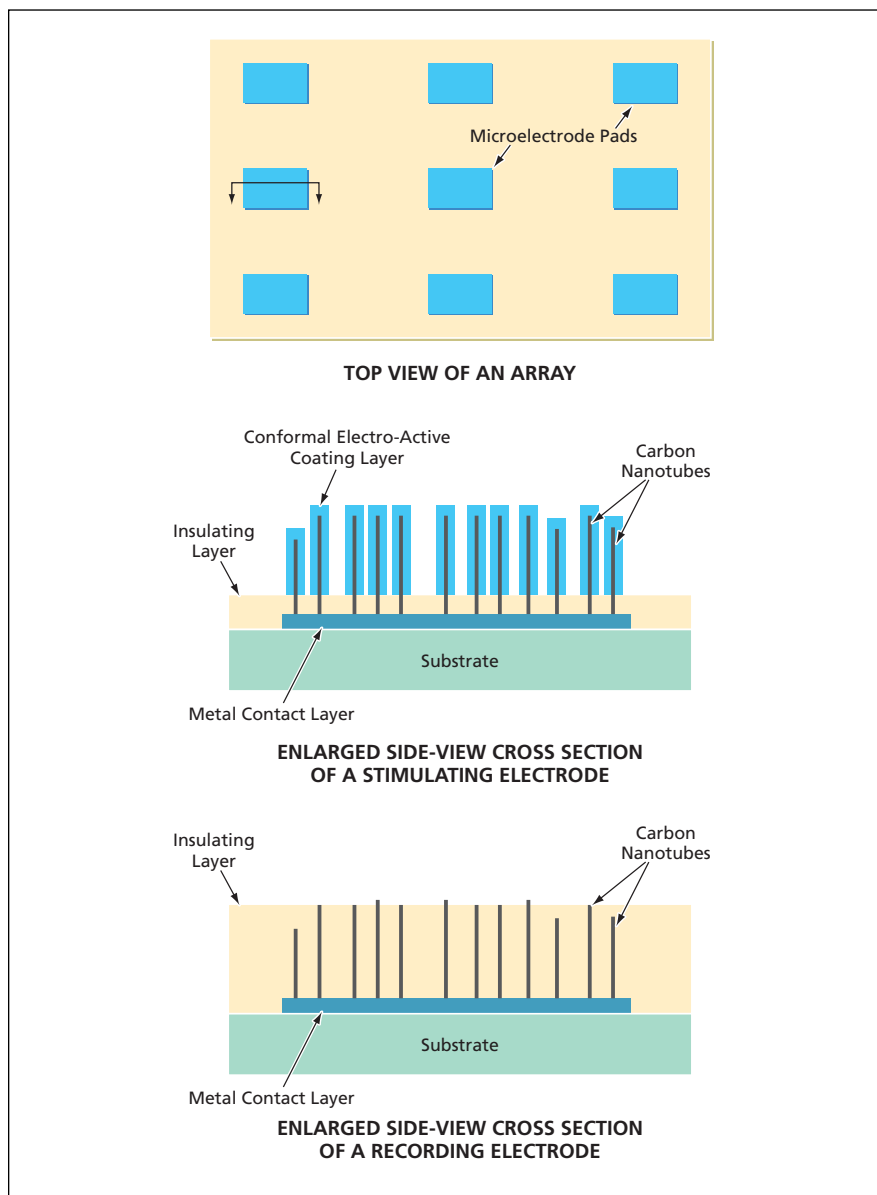
Ames Research Center, Moffett Field, California

A nanotube array based on vertically aligned nanotubes or carbon nanofibers has been invented for use in localized electrical stimulation and recording of electrical responses in selected regions of an animal body, especially including the brain. There are numerous estab-

lished, emerging, and potential applications for localized electrical stimulation and/or recording, including treatment of Parkinson's disease, Tourette's syndrome, and chronic pain, and research on electrochemical effects involved in neurotransmission.

Carbon-nanotube-based electrodes offer potential advantages over metal macroelectrodes (having diameters of the order of a millimeter) and microelectrodes (having various diameters ranging down to tens of microns) heretofore used in such applications. These advantages include the following:

- Stimuli and responses could be localized at finer scales of spatial and temporal resolution, which is at subcellular level, with fewer disturbances to, and less interference from, adjacent regions.
- There would be less risk of hemorrhage on implantation because nanoelectrode-based probe tips could be configured to be less traumatic.
- Being more biocompatible than are metal electrodes, carbon-nanotube-based electrodes and arrays would be more suitable for long-term or permanent implantation.
- Unlike macro- and microelectrodes, a nanoelectrode could penetrate a cell membrane with minimal disruption. Thus, for example, a nanoelectrode could be used to generate an action potential inside a neuron or in proximity of an active neuron zone. Such stimulation may be much more effective than is extra- or intracellular stimulation via a macro- or microelectrode.
- The large surface area of an array at a micron-scale footprint of non-insulated nanoelectrodes coated with a suitable electrochemically active material containing redox ingredients would make it possible to obtain a pseudocapacitance large enough to dissipate a relatively large amount of electric charge, so that a large stimulation current could be applied at a micron-scale region without exhausting the redox ingredients.
- Carbon nanotube array is more compatible with the three-dimensional network of tissues. Particularly, a better electrical-neural interface can be formed.
- A carbon nanotube array inlaid in insulating materials with only the ends exposed is an extremely sensitive electroanalysis tool that can measure the local neurotransmitter signal at extremely high sensitivity and temporal resolution.



Carbon Nanotubes connected to metal contact layers would protrude from surfaces of microelectrode pads. In use, the array would be positioned so that at least some nanotubes would be in electrical contact with cell components or intercellular structures of interest.

A nanoelectrode array according to the invention (see figure) would include two or more microelectrode pads on an electrically insulating substrate. The sizes of the microelectrode pads and the distances between them could range from as little as about a micron to as large as hundreds of microns, the exact values depending on the intended use. Each microelectrode pad could be electrically addressed, either individually or in combination with one or more other pads for localized stimulation and/or recording. Each microelectrode pad would support either a stimulating or a recording electrode. In either case, the electrode would comprise a subarray of multiple nanoelectrodes in the form of carbon nanotubes electrically connected to, and protruding perpendicularly from, a metal contact layer on an electrically insulating substrate.

In the case of a stimulating electrode, the protruding portions of the carbon nanotubes would be treated to deposit a thin electro-active coating layer that

would impart the desired amount of pseudocapacitance. Depending on the application, the exposed surface of the metal contact layer between the nanoelectrodes would be coated with an electrically insulating material (e.g., silica or a nonconductive polymer), or with an electrically conductive or electro-active polymer.

In the case of a recording electrode, it is desirable to minimize the size of the electrically exposed portion of each carbon nanotube so as to maximize the degree of localization and to minimize noise (thereby maximizing sensitivity). Therefore, an insulating layer would be deposited to sufficient thickness that only the tip(s) of the longest carbon nanotube(s) would protrude.

The term carbon nanotube here covers a general class of carbon materials, including multi-walled carbon nanotubes (MWCNTs) and nanofibers (CNFs). These nanostructured carbon materials have physical and chemical properties that make them especially

suitable for use as nanoelectrodes according to this invention. Well-aligned arrays of MWCNTs/CNFs have been grown by plasma-enhanced chemical vapor deposition on metal lines that have been pre-patterned by use of lithographic techniques. A previously published "bottom-up" scheme for fabricating an array of MWCNTs/CNFs that protrude from metal lines embedded in an SiO₂ matrix has been adopted as the basis of a scheme for fabricating nanoelectrode arrays according to the invention. The fabrication processes involved in these schemes are compatible with those used in manufacturing semiconductor devices. Hence, it should be possible to fabricate the nanoelectrode arrays at relatively low cost.

This work was done by Jun Li and M. Meyyappan of Ames Research Center and Russell Andrews, an Ames associate.

Inquiries concerning rights for the commercial use of this invention should be addressed to the Ames Innovative Partnerships Office at (650) 604-2954. Refer to ARC-15062-1.

Compact Directional Microwave Antenna for Localized Heating

Heating is concentrated on one side.

Lyndon B. Johnson Space Center, Houston, Texas

A directional, catheter-sized cylindrical antenna has been developed for localized delivery of microwave radiation for heating (and thus killing) diseased tissue without excessively heating nearby healthy tissue. By "localized" is meant that the antenna radiates much more in a selected azimuthal direction than in the opposite radial direction, so that it heats tissue much more on one side than it does on the opposite side. This antenna can be inserted using either a catheter or a syringe. A 2.4-mm prototype was tested, although smaller antennas are possible.

Prior compact, cylindrical antennas designed for therapeutic localized hyperthermia do not exhibit such directionality; that is, they radiate in approximately axisymmetric patterns. Prior directional antennas designed for the same purpose have been, variously, (1) too large to fit within catheters or (2) too large, after deployment from catheters, to fit within the confines of most human organs. In contrast, the present antenna offers a high degree of directionality and is compact enough to be useable as a catheter in some applications.

The antenna design is a hybrid of monopole-antenna and transmission-line design elements. The antenna (see Figure 1) is formed from an open-ended coplanar waveguide in which the gap between the middle conductor strip and the two outer (ground) conductor strips tapers from (1) a smaller value more characteristic of a transmission line to (2) a larger value more characteristic of a leaky transmission line or an antenna. The coplanar waveguide is wrapped around a polytetrafluoroethylene (PTFE) tube, and its abutting edges are soldered together to form the

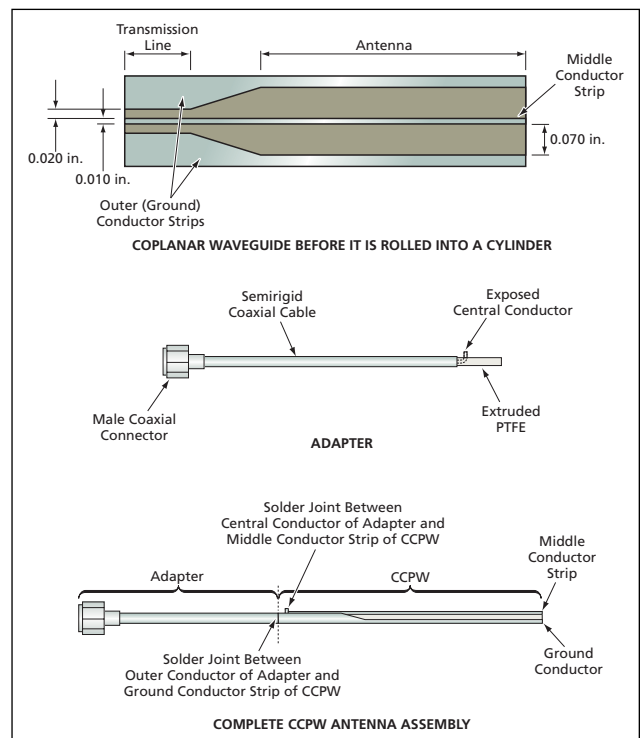


Figure 1. A Coplanar Waveguide With a Taper is rolled into a cylinder and joined with a coaxial-cable adapter to form a narrow antenna that radiates predominantly to one side.

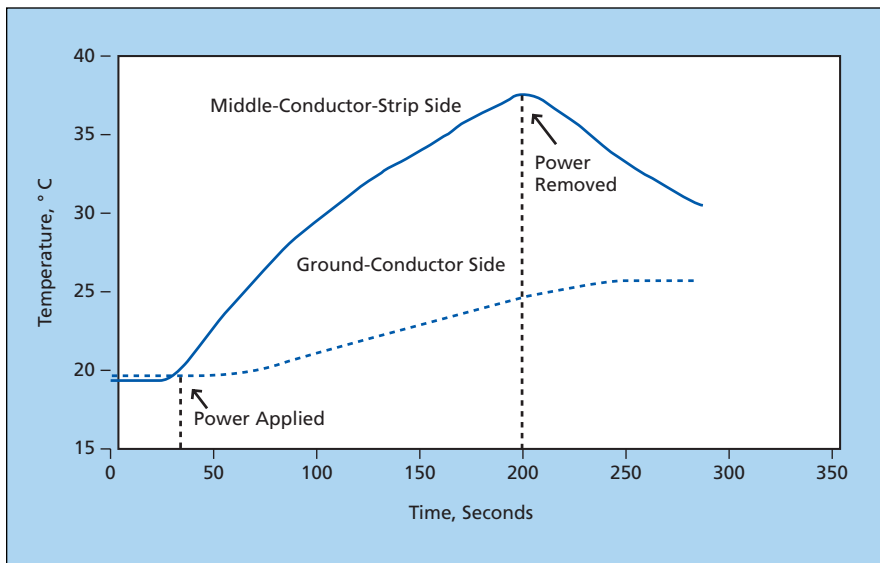


Figure 2. The **Temperature Rises on Opposite Sides** of the antenna were unequal, as desired, in a mass of simulated tissue heated with microwave power by use of the antenna.

cylindrical antenna structure, now denoted a cylindrical coplanar waveguide (CCPW), in which there is only one ground conductor. In operation, the wide-gap region between the middle conductor strip and the ground conductor permits radiation into the top side,

while the larger ground side limits radiation on the back side.

For a test of directionality, the antenna was inserted in a piece of biomedical simulation material, called “phantom” in the art, formulated to have thermal and electromagnetic properties similar to those of

human tissue. The phantom was instrumented with two fiber-optic temperature probes: one at 3 mm radially outward from the middle conductor of the CCPW and one 3 mm radially outward from the ground conductor on the opposite side. The catheter was excited with a power of 5 W at a frequency of 2.45 GHz. The temperature measurements, plotted in Figure 2, showed that, as desired, there was considerably more heating on the middle-conductor side. As indicated in Figure 2, the temperature difference between the targeted direction and the back side is about 13°C. This difference is sufficient to provide localized ablation (killing of targeted diseased cells) while preserving the healthy tissue.

This work was done by Patrick W. Fink, Gregory Y. Lin, Andrew W. Chu, Justin A. Dobbins, G. Dickey Arndt, and Phong Ngo of Johnson Space Center.

This invention is owned by NASA, and a patent application has been filed. Inquiries concerning nonexclusive or exclusive license for its commercial development should be addressed to the Patent Counsel, Johnson Space Center, (281) 483-0837. Refer to MSC-23781.

Using Hyperspectral Imagery To Identify Turfgrass Stresses

Stress maps could enable more-efficient management of large turfgrass fields.

Stennis Space Center, Mississippi

The use of a form of remote sensing to aid in the management of large turfgrass fields (e.g. golf courses) has been proposed. A turfgrass field of interest would be surveyed in sunlight by use of an airborne hyperspectral imaging system, then the raw observational data would be preprocessed into hyperspectral reflectance image data. These data would be further processed to identify turfgrass stresses, to determine the spatial distributions of those stresses, and to generate maps showing the spatial distributions.

Until now, chemicals and water have often been applied, variously, (1) indiscriminately to an entire turfgrass field without regard to localization of specific stresses or (2) to visible and possibly localized signs of stress — for example, browning, damage from traffic, or conspicuous growth of weeds. Indiscriminate application is uneconomical and environmentally unsound; the amounts of water and chemicals consumed could be insufficient in some

areas and excessive in most areas, and excess chemicals can leak into the environment. In cases in which developing stresses do not show visible signs at first, it could be more economical and effective to take corrective action before visible signs appear. By enabling early identification of specific stresses and their locations, the proposed method would provide guidance for planning more effective, more economical, and more environmentally sound turfgrass-management practices, including application of chemicals and water, aeration, and mowing.

The underlying concept of using hyperspectral imagery to generate stress maps as guides to efficient management of vegetation in large fields is not new; it has been applied in the growth of crops to be harvested. What is new here is the effort to develop an algorithm that processes hyperspectral reflectance data into spectral indices specific to stresses in turfgrass. The development effort has included a

study in which small turfgrass plots that were, variously, healthy or subjected to a variety of controlled stresses were observed by use of a hand-held spectroradiometer. The spectroradiometer readings in the wavelength range from 350 to 1,000 nm were processed to extract hyperspectral reflectance data, which, in turn, were analyzed to find correlations with the controlled stresses. Several indices were found to be correlated with drought stress and to be potentially useful for identifying drought stress before visible symptoms appear.

This work was done by Kendall Hutto and David Shaw of Mississippi State University for Stennis Space Center.

Inquiries concerning rights for its commercial use should be addressed to:

Mississippi State, MS 39762

Phone No.: (662) 325-9575

E-mail: dshaw@grl.msstate.edu

Refer to SSC-00270-1, volume and number of this NASA Tech Briefs issue, and the page number.



Shaping Diffraction-Grating Grooves To Optimize Efficiency

Spectral response of a grating could be tailored to complement responses of other components.

NASA's Jet Propulsion Laboratory, Pasadena, California

A method of shaping diffraction-grating grooves to optimize the spectral efficiency, spectral range, and image quality of a spectral imaging instrument is under development. The method is based on the use of an advanced design algorithm to determine the possibly complex shape of grooves needed to obtain a desired efficiency-versus-wavelength response (see figure). Then electron-beam fabrication techniques are used to realize the required groove shape. The method could be used, for example, to make the spectral efficiency of the grating in a given wavelength range proportional to the inverse of the spectral efficiency of a photodetector

array so that the overall spectral efficiency of the combination of the grating and the photodetector array would be flat. The method has thus far been applied to one-dimensional gratings only, but in principle, it is also applicable to two-dimensional gratings.

The algorithm involves calculations in the spatial-frequency domain. The spatial-frequency spectrum of a grating is represented as a diffraction-order spectral-peak-width function multiplied by an efficiency function for a single grating groove. This representation affords computational efficiency and accuracy by making it possible to consider only the response from one grating

groove (one period of the grating), instead of from the whole grating area, in determining the response from the entire grating. This combination of efficiency and accuracy is crucial for future extensions of the algorithm to two-dimensional designs and to designs in which polarization must also be taken into account.

The algorithm begins with the definition of target values of relative efficiency that represent the desired spectral response of the grating in certain spectral frequencies calculated from the diffraction order and wavelength. The grating period is divided into a number of cells — typically, 100. The phase contribution from each cell is determined from the phase of the incident electromagnetic wave and the height of the grating surface in the cell. The total contribution from all cells to each target value is then calculated. Then a method known to specialists as the optimum-rotation-angle method is used to adjust the height of each cell so that the total response from all cells is optimized. The computation is iterative and continues until the desired response is obtained. In the event that the desired response is unphysical, the algorithm nevertheless strives to generate a grating-groove profile for which the response approximates the desired one as closely as possible.

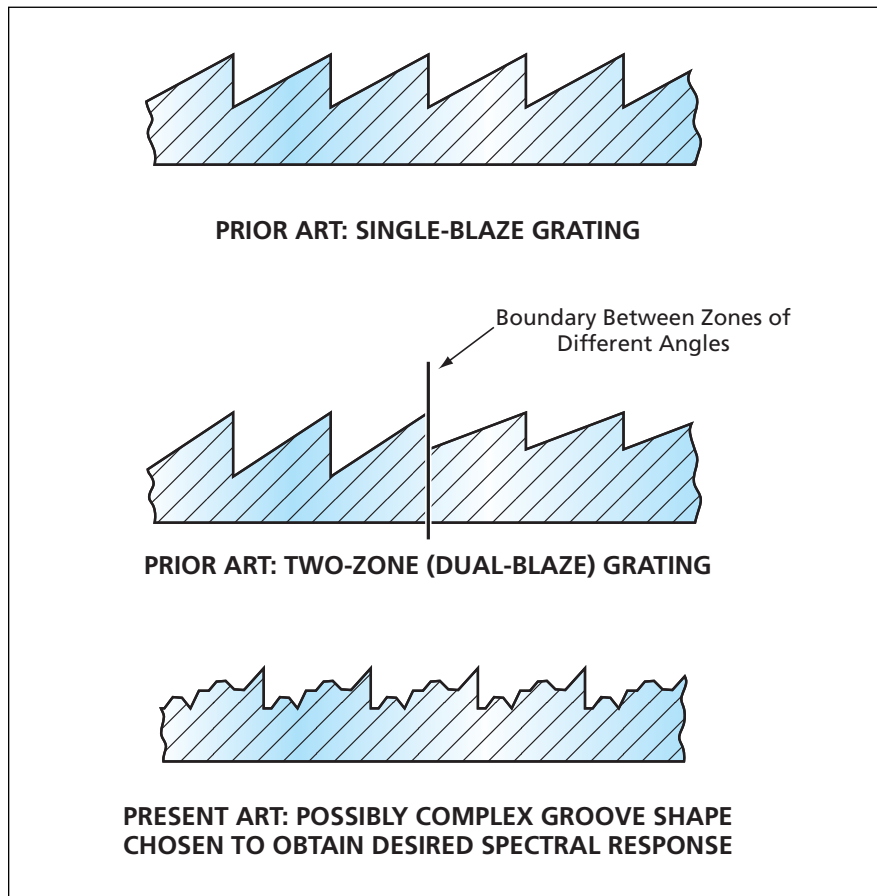
This work was done by John Backlund, Daniel Wilson, Pantazis Mouroulis, Paul Maker, and Richard Muller of NASA's Jet Propulsion Laboratory. Further information is contained in a TSP (see page 1).

In accordance with Public Law 96-517, the contractor has elected to retain title to this invention. Inquiries concerning rights for its commercial use should be addressed to:

*Innovative Technology Assets Management
JPL
Mail Stop 202-233
4800 Oak Grove Drive
Pasadena, CA 91109-8099
(818) 354-2240*

E-mail: iaoffice@jpl.nasa.gov

Refer to NPO-40429, volume and number of this NASA Tech Briefs issue, and the page number.



All of the Grooves of a Grating are designed to have the same possibly complex shape, which is chosen in an iterative process to obtain a desired spectral response. This approach offers greater design flexibility than does a prior method of tailoring the spectral response of a grating by dividing the grating into two or more zones that contain conventional sawtooth grooves having different blaze angles.

Low-Light-Shift Cesium Fountain Without Mechanical Shutters

Light shift is reduced by a combination of detuning and attenuation.

NASA's Jet Propulsion Laboratory, Pasadena, California

A new technique for reducing errors in a laser-cooled cesium fountain frequency standard provides for strong suppression of the light shift without need for mechanical shutters. Because mechanical shutters are typically susceptible to failure after operating times of the order of months, the elimination of mechanical shutters could contribute significantly to the reliability of frequency standards that are required to function continuously for longer time intervals.

With respect to the operation of an atomic-fountain frequency standard, the term "light shift" denotes an undesired relative shift in the two energy levels of the atoms (in this case, cesium atoms) in the atomic fountain during interrogation by microwaves. The shift in energy levels translates to a frequency shift that reduces the precision and possibly accuracy of the frequency standard. For reasons too complex to describe within the space available for this article, the light shift is caused by any laser light that reaches the atoms during the microwave-interrogation period, but is strongest for near-resonance light. In the absence of any mitigating design feature, the light shift, expressed as a fraction of the standard's frequency, could

be as large as $\approx 2 \times 10^{-11}$, the largest error in the standard.

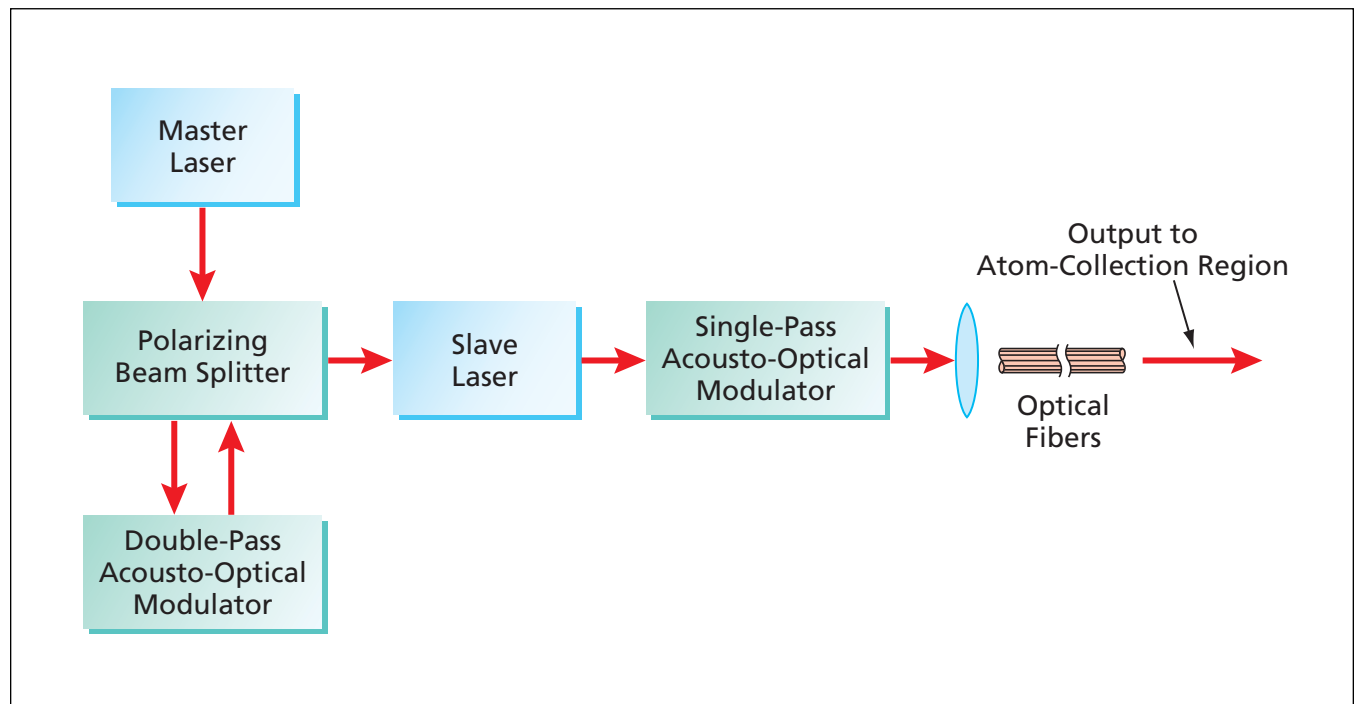
In a typical prior design, to suppress light shift, the intensity of laser light is reduced during the interrogation period by using a single-pass acousto-optic modulator to deflect the majority of light away from the main optical path. Mechanical shutters are used to block the remaining undeflected light to ensure complete attenuation. Without shutters, this remaining undeflected light could cause a light shift of as much as $\approx 10^{-15}$, which is unacceptably large in some applications.

The new technique implemented here involves additionally shifting the laser wavelength off resonance by a relatively large amount (typically of the order of nanometers) during microwave interrogation. In this design, when microwave interrogation is not underway, the atoms are illuminated by a slave laser locked to the lasing frequency of a lower power master laser. The locking is achieved by injecting a small amount of master laser light into the slave laser. This light is injected via a polarizing beam splitter after passing through a double-pass acousto-optic modulator (see figure). The output of

the slave laser is then sent through the single-pass acousto-optic modulator mentioned above to optical fibers that, in turn, feed the light to the collection region of the atomic fountain.

During microwave interrogation, the radio-frequency power applied to the double-pass acousto-optic modulator is turned off in order to cut off the injection light and detune the slave laser to its free-running wavelength, which is typically nanometers away from the resonant master laser. Even in the absence of other measures, this tuning away from resonance reduces the light shift by about four orders of magnitude. Further cutting the radio-frequency power to the single-pass acousto-optic modulator causes attenuation of the slave-laser output beam. It has been verified experimentally that this combination of frequency shift and attenuation reduces the light shift to $< 10^{-15}$, and it has been estimated that the resultant shift could be as low as 2×10^{-19} .

This work was done by William Klipstein and Daphna Enzer of Caltech for NASA's Jet Propulsion Laboratory. For more information, contact iaoffice@jpl.nasa.gov. NPO-42136



Laser illumination of atoms in the collection region of an atomic fountain is shifted away from the resonance frequency (by use of the double-pass acousto-optical modulator) and attenuated (by use of the single-pass acousto-optical modulator) during microwave interrogation.

Magnetic Compensation for Second-Order Doppler Shift in LITS

Fractional frequency stability could be the lowest ever achieved.

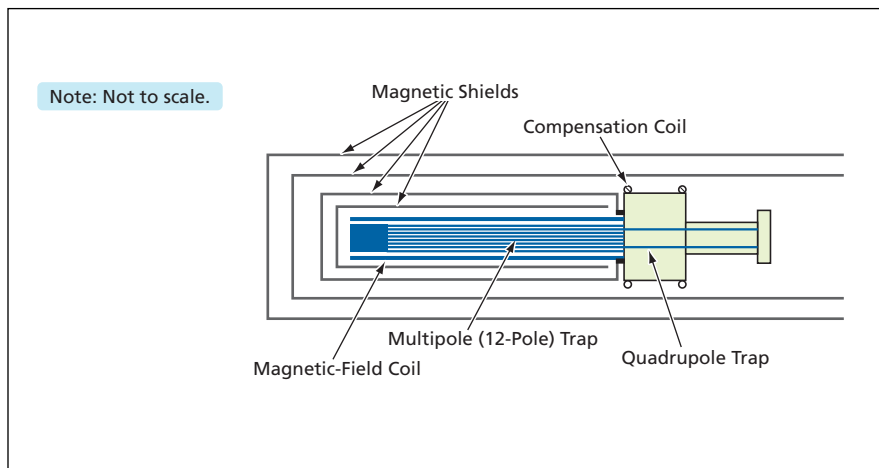
NASA's Jet Propulsion Laboratory, Pasadena, California

The uncertainty in the frequency of a linear-ion-trap frequency standard (LITS) can be reduced substantially by use of a very small magnetic inhomogeneity tailored to compensate for the residual second-order Doppler shift. An effect associated with the relativistic time dilatation, one cause of the second-order Doppler shift, is ion motion that is attributable to the trapping radio-frequency (RF) electromagnetic field used to trap ions. The second-order Doppler shift is reduced by using a multi-pole trap; however it is still the largest source of systematic frequency shift in the latest generation of LITSs, which are among the most stable clocks in the world. The present compensation scheme reduces the frequency instability of the affected LITS to about a tenth of its previous value.

The basic principles of prior generation LITSs were discussed in several prior *NASA Tech Briefs* articles. Below are recapitulated only those items of basic information necessary to place the present development in context. A LITS includes a microwave local oscillator, the frequency of which is stabilized by comparison with the frequency of the ground state hyperfine transition of $^{199}\text{Hg}^+$ ions. The comparison involves a combination of optical and microwave excitation and interrogation of the ions in a linear ion trap in the presence of a nominally uniform magnetic field.

In the current version of the LITS, there are two connected traps (see figure): (1) a quadrupole trap wherein the optical excitation and measurement take place and (2) a 12-pole trap (denoted the resonance trap), wherein the microwave interrogation takes place. The ions are initially loaded into the quadrupole trap and are thereafter shuttled between the two traps. Shuttling ions into the resonance trap allows sensitive microwave interrogation to take place well away from loading interference. The axial magnetic field for the resonance trap is generated by an electric current in a finely wound wire coil surrounded by magnetic shields.

In the quadrupole and 12-pole traps, the potentials are produced by RF voltages applied to even numbers (4 and 12, respectively) of parallel rods equally spaced around a circle. The polarity of the voltage on each rod is opposite that



A Typical Latest-Generation Multipole LITS contains a quadrupole trap and another multipole (e.g., 12-pole) trap surrounded by a coil that generates a nominally uniform axial magnetic field. In the present compensation scheme, a controlled magnetic inhomogeneity is introduced by use of a compensation coil.

of the voltage on the adjacent rod. As a result, the amplitude of the RF trapping field is zero along the centerline and increases, with radius, to a maximum value near the rods.

As the number of ions temporally varies in a small range about a target value, space-charge repulsion causes the ensemble of ions to occupy a varying volume within the trap. The change in radial occupation results in a change in the time-averaged magnitude of the trapping RF field sampled by the ions and a change in ion micromotion amplitude, which will cause a corresponding change in the second-order Doppler shift. (The first-order Doppler shift is eliminated by the geometry of the trap and the polarization of interrogating microwave field.)

In a 12-pole trap, the ions are free particles for most of their trajectories, interacting with significant RF amplitude only at the edges of the trap. As a result, the time-averaged RF amplitude sampled by the ions is significantly smaller, for the same number of ions trapped, than it is in a typical quadrupole trap used in an earlier-generation LITS. The sensitivity to the second-order Doppler shift is more than 10 times smaller than in the case of a quadrupole-trap LITS, making the long-term stability of a 12-pole-trap LITS comparable to or even better than that of the best hydrogen masers. Nevertheless, the second-order Doppler shift remains the largest shift in the LITS, and the

problem is to reduce it even further.

As a solution to this problem, the present compensation scheme exploits the following facts:

- The ion-number-dependent second-order Doppler shift is negative and increases in magnitude as the number of ions increases.
- Heretofore, in designing a LITS, great care has been taken to provide a uniform magnetic field within the trap so that as the volume occupied by the ions changes, the average magnetic field sampled by the ions does not change.
- Notwithstanding the nominal uniformity of the magnetic field as described above, it is possible to introduce a well-controlled magnetic-field inhomogeneity, such that ions in a changing occupation volume sample a slightly different magnetic field. The resulting inhomogeneity in the second-order Zeeman shift can be used to counteract the second-order Doppler shift.

Accordingly, in the present compensation scheme, one or more coaxial compensation coil(s) is or are used to generate one or more small magnetic-field inhomogeneities. The placement of, and currents in, the coils can be chosen to obtain either a positive or negative change in the second-order Zeeman shift with a change in the number of ions. By careful adjustment of the current(s) in the compensation coil(s), the

second order Zeeman shift can be made to almost exactly cancel the residual second-order Doppler shift.

In an experimental implementation of this scheme, a 5-turn compensation coil was placed between the quadrupole and 12-pole traps and was excited

with a current of 3 mA. With this compensation scheme, the measured fractional frequency stability of the second-order Doppler shift is 3×10^{-17} . As a result, all systematics in the clock, and the clock itself, should have a long-term stability of better than 5×10^{-17} ,

which would be the best ever measured in any clock.

This work was done by Eric Burt and Robert Tjoelker of Caltech for NASA's Jet Propulsion Laboratory. For more information, contact iaoffice@jpl.nasa.gov NPO-43199

Nanostructures Exploit Hybrid-Polariton Resonances

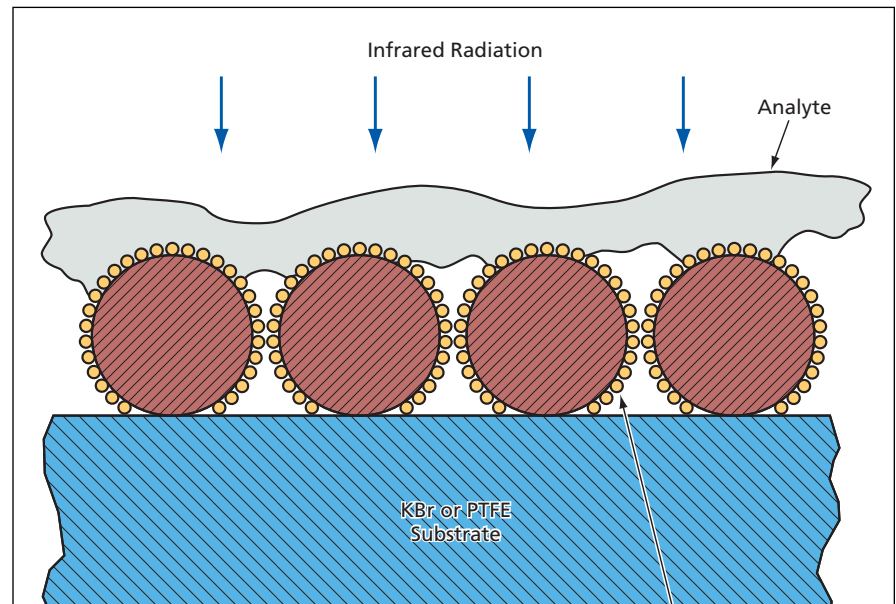
Infrared absorption or scattering by molecules of interest can be greatly enhanced.

NASA's Jet Propulsion Laboratory, Pasadena, California

Nanostructured devices that exploit the hybrid-polariton resonances arising from coupling among photons, phonons, and plasmons are subjects of research directed toward the development of infrared-spectroscopic sensors for measuring extremely small quantities of molecules of interest. The spectroscopic techniques in question are surface enhanced Raman scattering (SERS) and surface enhanced infrared absorption (SEIRA). An important intermediate goal of this research is to increase the sensitivity achievable by these techniques. The basic idea of the approach being followed in this research is to engineer nanostructured devices and thereby engineer their hybrid-polariton resonances to concentrate infrared radiation incident upon their surfaces in such a manner as to increase the absorption of the radiation for SEIRA and measure the frequency shifts of surface vibrational modes.

The underlying hybrid-polariton-resonance concept is best described by reference to experimental devices that have been built and tested to demonstrate the concept. The nanostructure of each such device includes a matrix of silicon carbide particles of approximately 1 micron in diameter that are supported on a potassium bromide (KBr) or poly(tetrafluoroethylene) [PTFE] window. These grains are sputter-coated with gold grains of 40-nm size (see figure).

From the perspective of classical electrodynamics, in this nanostructure, that includes a particulate or otherwise rough surface, the electric-field portion of an incident electromagnetic field becomes concentrated on the particles when optical resonance conditions are met. Going beyond the perspective of classical electrodynamics, it can be seen that when the resonance frequencies of surface phonons and surface plasmons overlap, the coupling of the resonances



Circumferential Belts were formed by diamond turning on the initially cylindrical surface of a CaF₂ rod. The radial depths and axial widths of the belts were chosen to make some of the belts act as single-mode and some as multi-mode WGM resonators.

gives rise to an enhanced radiation-absorption or -scattering mechanism.

The sizes, shapes, and aggregation of the particles determine the frequencies of the resonances. Hence, the task of designing a nanostructure to exhibit the desired radiation-absorption properties translates, in large part, to selecting particle sizes and shapes to obtain the desired enhanced coupling of energy from photons to plasmons and phonons. To broaden the spectral region(s) of enhanced absorption, one would select a distribution of particle sizes and shapes.

In a test, the infrared spectra of one of the experimental nanostructures described above were measured before and after the nanostructure was coated with an approximately-monomolecular-thickness layer of poly(methyl methacrylate) [PMMA]. Among other things, the measurements showed that in the af-

fected wavelength range, in the presence of the nanostructure, the magnitude of absorption by the thin PMMA film was comparable to the absorption by a considerably thicker PMMA film without the nanostructure.

This work was done by Mark Anderson of Caltech for NASA's Jet Propulsion Laboratory.

In accordance with Public Law 96-517, the contractor has elected to retain title to this invention. Inquiries concerning rights for its commercial use should be addressed to:

*Innovative Technology Assets Management
JPL*

*Mail Stop 202-233
4800 Oak Grove Drive
Pasadena, CA 91109-8099
(818) 354-2240*

E-mail: iaoffice@jpl.nasa.gov

Refer to NPO-42341, volume and number of this NASA Tech Briefs issue, and the page number.

Microfluidics, Chromatography, and Atomic-Force Microscopy

Capillary and shear effects are exploited to transport small quantities of liquids.

NASA's Jet Propulsion Laboratory, Pasadena, California

A Raman-and-atomic-force microscope (RAFM) has been shown to be capable of performing several liquid-transfer and sensory functions essential for the operation of a microfluidic “laboratory on a chip” that would be used to perform rapid, sensitive chromatographic and spectro-chemical analyses of unprecedentedly small quantities of liquids. The most novel aspect of this development lies in the exploitation of capillary and shear effects at the atomic-force-microscope (AFM) tip to produce shear-driven flow of liquids along open microchannels of a microfluidic device. The RAFM can also be used to perform such functions as imaging liquids in microchannels; removing liquid samples from channels for very sensitive, tip-localized spectrochemical analyses; measuring a quantity of liquid adhering to the tip; and dip-pen deposition from a chromatographic device.

A commercial Raman-spectroscopy system and a commercial AFM were integrated to make the RAFM so as to be able to perform simultaneous topographical AFM imaging and surface-enhanced Raman spectroscopy (SERS) at the AFM tip. The Raman-spectroscopy system includes a Raman microprobe attached to an optical microscope, the translation stage of which is modified to accommodate the AFM head. The Raman laser excitation beam, which is aimed at the AFM tip, has a wavelength of 785 nm and a diameter of about 5 μm , and its power is adjustable up to 10 mW. The AFM is coated with gold to enable tip-localized SERS.

Heretofore, the use of microfluidic devices for “laboratory on a chip” applications has been inhibited by the need for very high pressures to pump fluids through capillary channels at sufficient rates. Shear-driven flow offers an alternative by eliminating the need for pressure. In the basic form of shear-driven pumping, illustrated at the top of Figure 1, two parallel plates with a liquid between them are driven laterally with respect to each other, causing the liquid to be pumped between the plates. Shear-driven pumping makes it possible to produce very rapid flows along very narrow channels aligned along the sliding direction. The basic form of shear-driven pumping is used in shear-driven chromatography (SDC), in which the stationary plate is

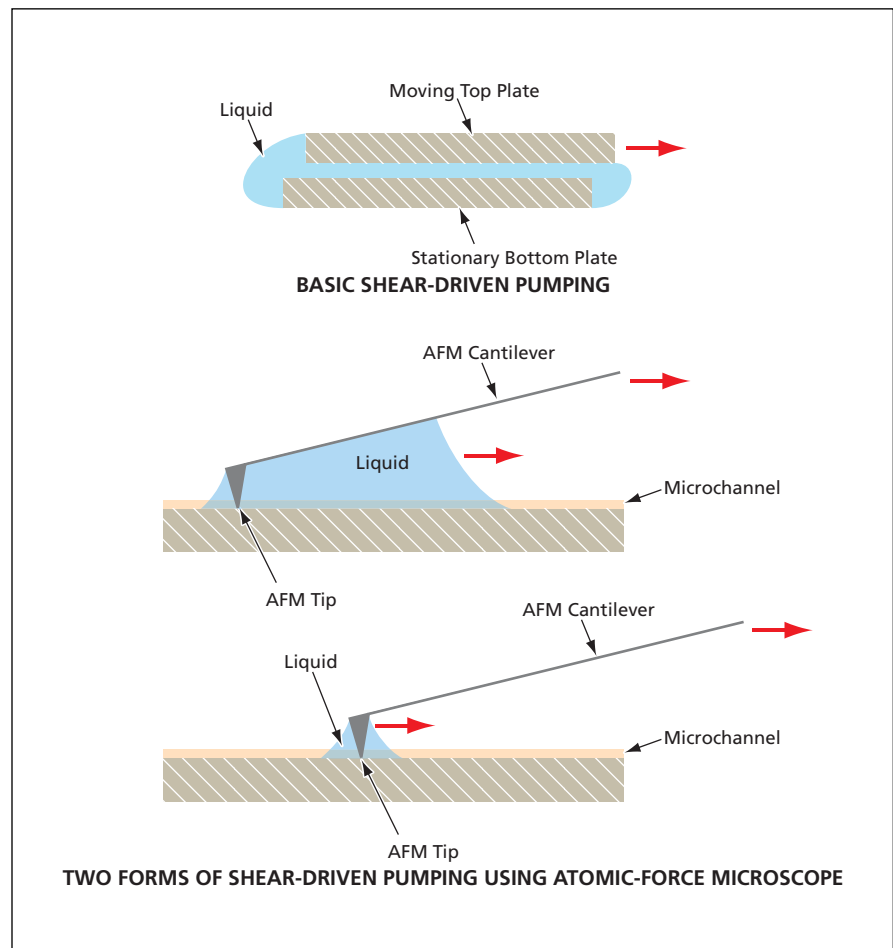


Figure 1. Shear-Driven Pumping is a viable technique for moving small quantities of liquid rapidly along a microchannel.

functionalized to effect chromatographic separation. In the present approach to shear-driven pumping, illustrated at the middle and bottom of Figure 1, liquid adhering to the RAFM tip and cantilever (or to the tip only) is simply dragged along a microchannel by moving the tip as in normal AFM operation.

In addition to moving a sample of liquid along a microchannel, the RAFM could be used to perform several other operations:

- A sample of liquid could be removed from a microchannel and placed in another microchannel.
- A sample of liquid clinging to the RAFM tip after removal from a microchannel could be subjected to SERS to determine its chemical composition.
- The RAFM could be operated as a con-

ventional AFM in a tapping mode to topographically map the surface of a liquid in a microchannel.

- The change in frequency of vibration of the cantilever-and-tip structure could be measured to determine the mass of liquid clinging to the tip.
- In a generalization from the concept of dip-pen nanolithography, one could perform dip-pen microchromatography, in which a chromatographic liquid would be discharged from a microchromatographic column at the base of the cantilever as the AFM tip was moved along a microchannel (see Figure 2). The liquid would flow along the cantilever onto the tip and would be deposited in the microchannel. After evaporation of the eluent (solvent), the resulting deposits of analytes along the channel could be analyzed

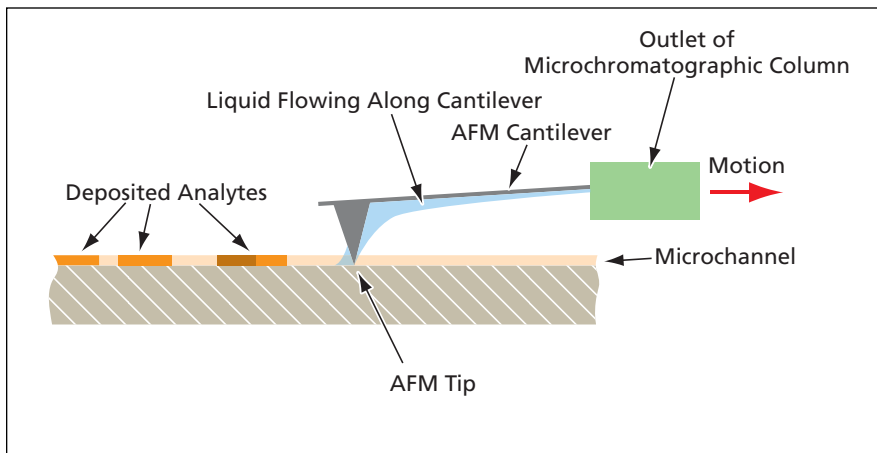


Figure 2. The **Moving AFM Tip** would deposit the outflow of a microchromatography column along a microchannel. After subsequent evaporation of the solvent, the AFM could be used to profile the deposited analytes.

by conventional AFM profiling.

This work was done by Mark Anderson of Caltech for NASA's Jet Propulsion Laboratory.

In accordance with Public Law 96-517, the contractor has elected to retain title to this invention. Inquiries concerning rights for its commercial use should be addressed to:

*Innovative Technology Assets Management
JPL*

*Mail Stop 202-233
4800 Oak Grove Drive
Pasadena, CA 91109-8099
(818) 354-2240*

E-mail: iaoffice@jpl.nasa.gov

Refer to NPO-41431, volume and number of this NASA Tech Briefs issue, and the page number.

Model of Image Artifacts From Dust Particles

This first-order geometric-optics-based model yields realistic predictions.

NASA's Jet Propulsion Laboratory, Pasadena, California

A mathematical model of image artifacts produced by dust particles on lenses has been derived. Machine-vision systems often have to work with camera lenses that become dusty during use. Dust particles on the front surface of a lens produce image artifacts that can potentially affect the performance of a machine-vision algorithm. The present

model satisfies a need for a means of synthesizing dust image artifacts for testing machine-vision algorithms for robustness (or the lack thereof) in the presence of dust on lenses.

A dust particle can absorb light or scatter light out of some pixels, thereby giving rise to a dark dust artifact. It can also scatter light into other pixels,

thereby giving rise to a bright dust artifact. For the sake of simplicity, this model deals only with dark dust artifacts. The model effectively represents dark dust artifacts as an attenuation image consisting of an array of diffuse darkened spots centered at image locations corresponding to the locations of dust particles. The dust artifacts are computa-

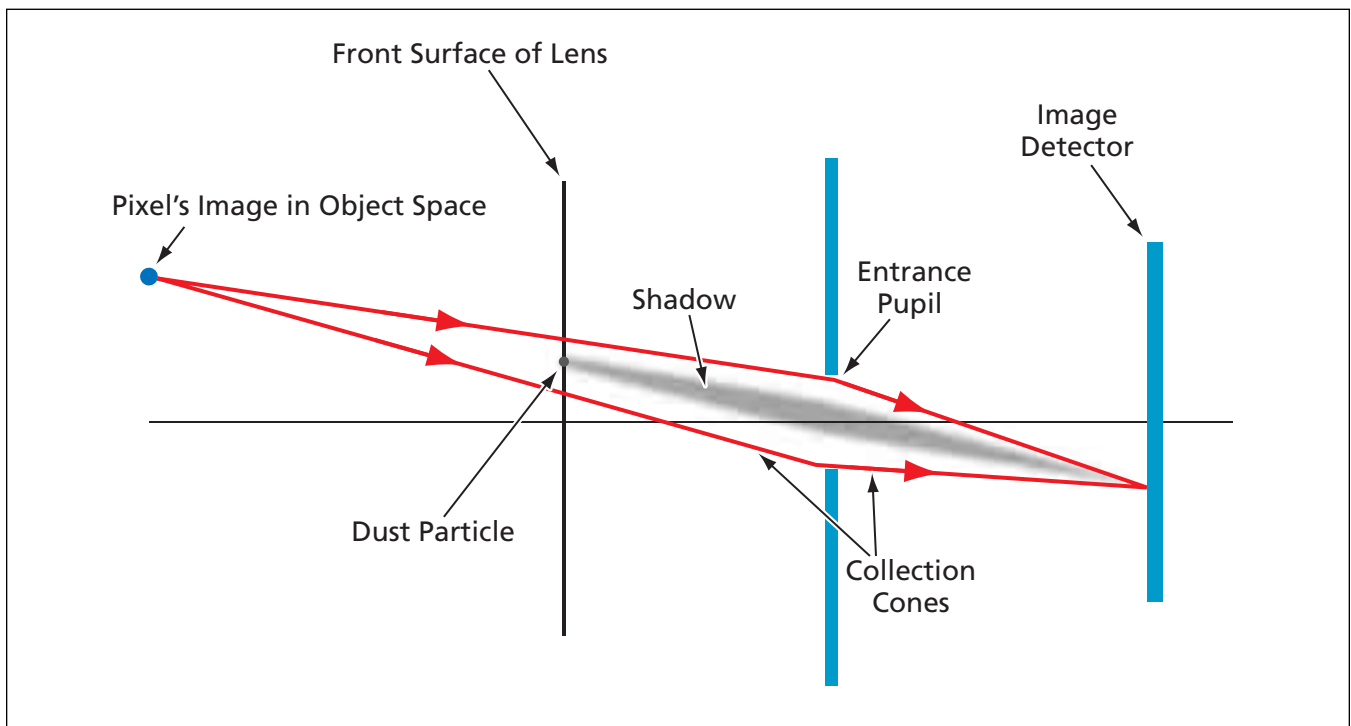


Figure 1. A **Geometric-Optics Model** of shadowing is used to compute the effects of dust particles on an image.

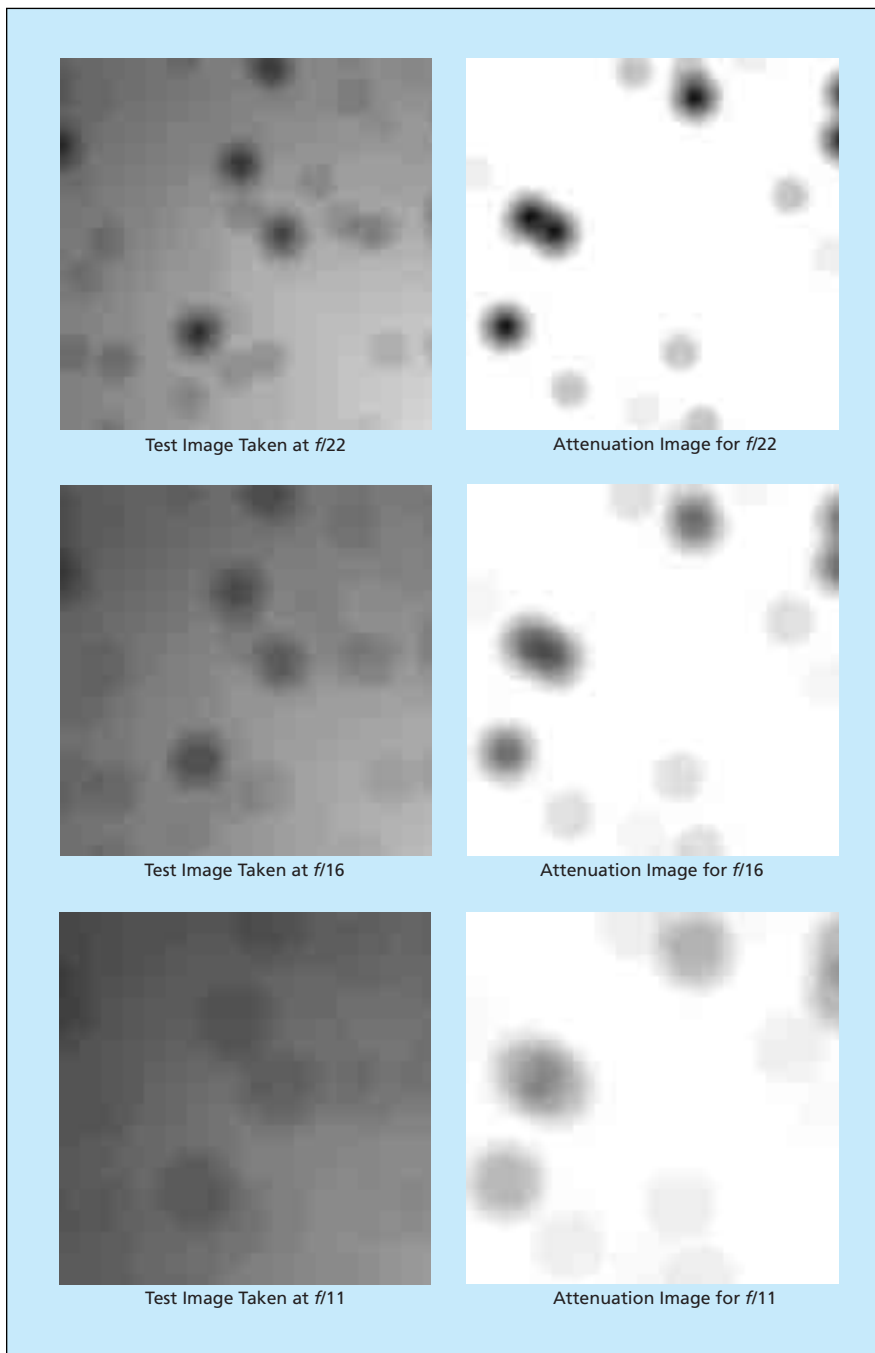


Figure 2. **Test Images Containing Dust Artifacts** recorded at various relative apertures are shown alongside the corresponding synthetic attenuation images.

tionally incorporated into a given test image by simply multiplying the brightness value of each pixel by a transmission factor that incorporates the factor of attenuation, by dust particles, of the light incident on that pixel.

With respect to computation of the attenuation and transmission factors, the model is based on a first-order geometric (ray)-optics treatment of the shadows cast by dust particles on the image detector. In this model, the light collected by a pixel is deemed to be confined to a pair of cones defined by the location of the pixel's image in object space, the entrance pupil of the lens, and the location of the pixel in the image plane (see Figure 1). For simplicity, it is assumed that the size of a dust particle is somewhat less than the diameter, at the front surface of the lens, of any collection cone containing all or part of that dust particle. Under this assumption, the shape of any individual dust particle artifact is the shape (typically, circular) of the aperture, and the contribution of the particle to the attenuation factor for a given pixel is the fraction of the cross-sectional area of the collection cone occupied by the particle. Assuming that dust particles do not overlap, the net transmission factor for a given pixel is calculated as one minus the sum of attenuation factors contributed by all dust particles affecting that pixel.

In a test, the model was used to synthesize attenuation images for random distributions of dust particles on the front surface of a lens at various relative aperture (F-number) settings. As shown in Figure 2, the attenuation images resembled dust artifacts in real test images recorded while the lens was aimed at a white target.

This work was done by Reg Willson of Caltech for NASA's Jet Propulsion Laboratory.

The software used in this innovation is available for commercial licensing. Please contact Karina Edmonds of the California Institute of Technology at (818) 393-2827. Refer to NPO-42437.



Pattern-Recognition System for Approaching a Known Target

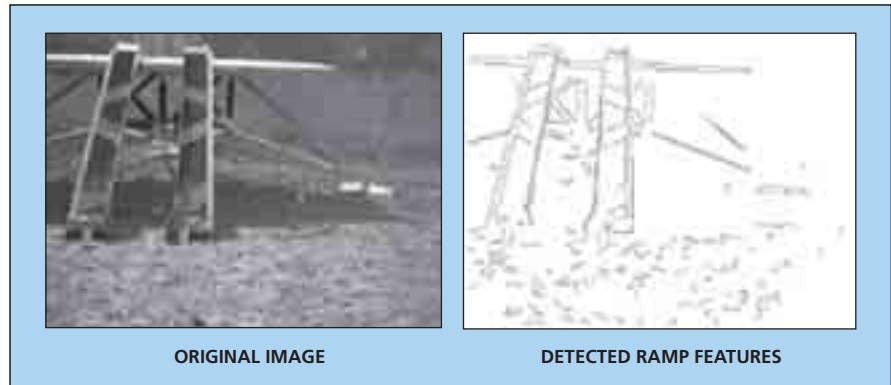
Multiple image features are utilized in a multiphase data-fusion process.

NASA's Jet Propulsion Laboratory, Pasadena, California

A closed-loop pattern-recognition system is designed to provide guidance for maneuvering a small exploratory robotic vehicle (rover) on Mars to return to a landed spacecraft to deliver soil and rock samples that the spacecraft would subsequently bring back to Earth. The system could be adapted to terrestrial use in guiding mobile robots to approach known structures that humans could not approach safely, for such purposes as reconnaissance in military or law-enforcement applications, terrestrial scientific exploration, and removal of explosive or other hazardous items.

The system has been demonstrated in experiments in which the Field Integrated Design and Operations (FIDO) rover (a prototype Mars rover equipped with a video camera for guidance) is made to return to a mockup of Mars-lander spacecraft. The FIDO rover camera autonomously acquires an image of the lander from a distance of 125 m in an outdoor environment. Then under guidance by an algorithm that performs fusion of multiple line and texture features in digitized images acquired by the camera, the rover traverses the intervening terrain, using features derived from images of the lander truss structure. Then by use of precise pattern matching for determining the position and orientation of the rover relative to the lander, the rover aligns itself with the bottom of ramps extending from the lander, in preparation for climbing the ramps to deliver samples to the lander.

The most innovative aspect of the system is a set of pattern-recognition algorithms that govern a three-phase visual-guidance sequence for approaching the lander. During the first phase, a multifeature fusion algorithm integrates the outputs of a horizontal-line-detection algorithm and a wavelet-transform-based visual-area-of-interest algorithm for detecting the lander from a significant distance. The horizontal-line-detection algorithm is used to determine candidate lander locations based on detection of a horizontal deck that is part of the lander. The wavelet transform is then performed on an acquired image, and a texture sig-



Features of the Ramps are used in close-range navigation.

nature is extracted in a local window of the wavelet coefficient space for each of the candidate lander locations. The multifeature fusion algorithm eliminates false positives arising from terrain features. The multifeature fusion algorithm is coupled with a three-dimensional visual-terminal-guidance algorithm that can extract and utilize cooperative features of the lander to accurately, iteratively estimate the pose of the rover relative to the lander and then steer the rover to the bottom of the ramps.

The second phase begins when the rover has arrived at ≈ 25 m from the lander and ends at a distance of ≈ 5 m. Inasmuch as the distance is more important than the position of the rover during this phase, the system utilizes parallel line features extracted from a truss structure that is part of the lander. In order to correctly distinguish the truss structure, the deck, which appears as a set of nearly level lines, is detected first. Any parallel lines below the deck are considered to be parts of the truss structure. Average distances between parallel lines are then used to estimate the distance from the rover to the lander, and the centroid of the parallel lines is used to compute the heading from the rover to the lander.

During the third phase, distinctive pattern of six stripes on the ramps is utilized in a close-range algorithm for positioning the rover within 10 cm of the bottom of the ramps. At the beginning of this phase, when the rover is ≈ 5 m from the lander,

the rover circles around the lander. The close-range algorithm includes three major steps: feature extraction, feature match, and pose estimation. The features are the six stripes, which are arranged so that any two of them is a topologically and spatially unique combination, so as to greatly reduce uncertainty and computational complexity.

An edge-detection subalgorithm is applied first. Then all straight-line segments are extracted. In order to find the stripes, the close-range algorithm looks for the ramps, which are defined by a set of long straight and nearly parallel lines (see figure). When a single stripe is detected in the image, a linear affine transformation based on its four corners can be constructed. If transformation provides a correct match with a known stripe, it can help to find other matches. A search on all stripes is performed to find the best matches. Once the matches are found, the position and orientation of the rover relative to the lander are estimated by use of the outside corners of the stripes. A minimum of four stripes is used to ensure safe navigation.

This work was done by Terrance Huntsberger and Yang Cheng of Caltech for NASA's Jet Propulsion Laboratory. Further information is contained in a TSP (see page 1).

The software used in this innovation is available for commercial licensing. Please contact Karina Edmonds of the California Institute of Technology at (626) 395-2322. Refer to NPO-41867.

➤ Orchestrator Telemetry Processing Pipeline

A multi-platform architecture is used to build and manage a telemetry-processing pipeline.

NASA's Jet Propulsion Laboratory, Pasadena, California

Orchestrator is a software application infrastructure for telemetry monitoring, logging, processing, and distribution. The architecture has been applied to support operations of a variety of planetary rovers. Built in Java with the Eclipse Rich Client Platform, Orchestrator can run on most commonly used operating systems. The pipeline supports configurable parallel processing that can significantly reduce the time needed to process a large volume of data products.

Processors in the pipeline implement a simple Java interface and declare their required input from upstream processors. Orchestrator is programmatically constructed by specifying a list of Java processor classes that are initiated at

runtime to form the pipeline. Input dependencies are checked at runtime. Fault tolerance can be configured to attempt continuation of processing in the event of an error or failed input dependency if possible, or to abort further processing when an error is detected.

This innovation also provides support for Java Message Service broadcasts of telemetry objects to clients and provides a file system and relational database logging of telemetry. Orchestrator supports remote monitoring and control of the pipeline using browser-based JMX controls and provides several integration paths for pre-compiled legacy data processors.

At the time of this reporting, the Orchestrator architecture has been used by

four NASA customers to build telemetry pipelines to support field operations. Example applications include high-volume stereo image capture and processing, simultaneous data monitoring and logging from multiple vehicles. Example telemetry processors used in field test operations support include vehicle position, attitude, articulation, GPS location, power, and stereo images.

This work was done by Mark Powell, David Mittman, Joseph Joswig, Thomas Crockett, and Jeffrey Norris of Caltech for NASA's Jet Propulsion Laboratory.

The software used in this innovation is available for commercial licensing. Please contact Karina Edmonds of the California Institute of Technology at (626) 395-2322. Refer to NPO-44561.

➤ Scheme for Quantum Computing Immune to Decoherence

The spintronic encodings of this scheme are more efficient than those of a prior scheme.

NASA's Jet Propulsion Laboratory, Pasadena, California

A constructive scheme has been devised to enable mapping of any quantum computation into a spintronic circuit in which the computation is encoded in a basis that is, in principle, immune to quantum decoherence. The scheme is implemented by an algorithm that utilizes multiple physical spins to encode each logical bit in such a way that collective errors affecting all the physical spins do not disturb the logical bit. The scheme is expected to be of use to experimenters working on spintronic implementations of quantum logic.

Spintronic computing devices use quantum-mechanical spins (typically, electron spins) to encode logical bits. Bits thus encoded (denoted qubits) are potentially susceptible to errors caused by noise and decoherence. The traditional model of quantum computation is based partly on the assumption that each qubit is implemented by use of a single two-state quantum system, such as an electron or other spin- $\frac{1}{2}$ particle. It can be surprisingly difficult to achieve certain gate operations — most notably, those of arbitrary

one-qubit gates — in spintronic hardware according to this model. However, ironically, certain two-qubit interactions (in particular, spin-spin exchange interactions) can be achieved relatively easily in spintronic hardware.

Therefore, it would be fortunate if it were possible to implement any one-qubit gate by use of a spin-spin exchange interaction. While such a direct representation is not possible, it is possible to achieve an arbitrary 1-qubit gate indirectly by means of a sequence of four spin-spin exchange interactions, which could be implemented by use of four exchange gates. Accordingly, the present scheme provides for mapping any one-qubit gate in the logical basis into an equivalent sequence of at most four spin-spin exchange interactions in the physical (encoded) basis. The complexity of the mathematical derivation of the scheme from basic quantum principles precludes a description within this article; it must suffice to report that the derivation provides explicit constructions for finding the exchange couplings in the physical basis needed to implement

any arbitrary one-qubit gate. These constructions lead to spintronic encodings of quantum logic that are more efficient than those of a previously published scheme that utilizes a universal but fixed set of gates.

Given this mapping, universal quantum computation could be achieved in the encoded basis if, in addition, it were also possible to implement a controlled-NOT (CNOT) gate in the encoded basis. It had been demonstrated in prior research that such encoded construction of a CNOT gate is possible. Hence, in the present scheme, the mapping of arbitrary one-qubit gates is augmented with the encoded construction of CNOT gates, making it theoretically possible to perform universal quantum computation in the encoded basis.

This work was done by Colin Williams and Farrokh Vatan of Caltech for NASA's Jet Propulsion Laboratory.

The software used in this innovation is available for commercial licensing. Please contact Karina Edmonds of the California Institute of Technology at (818) 393-2827. Refer to NPO-42996.



Books & Reports

Spin-Stabilized Microsatellites With Solar Concentrators

A document proposes the development of spin-stabilized microsatellites powered by solar photovoltaic cells aided by solar concentrators. Each such satellite would have a cylindrical or other axisymmetric main body with solar cells mounted in a circumferential beltlike array on its exterior surface. The solar concentrator would be a halo-like outrigger cylindrical Fresnel lens array that would be deployed from and would surround the main body, connected to the main body via spokes or similar structural members.

The spacecraft would be oriented with its axis of symmetry perpendicular to the line of sight to the Sun and would be set into rotation about this axis. In effect, the solar cells and concentrator would be oriented and rotated in a “rotisserie” mode, making it possible to take advantage of the concentration of solar light while preventing localized overheating of the solar cells. In addition, the mechanical stabilization inherently afforded by the rotation could be exploited as a means of passive attitude control or, at least, of reducing the requirement for active attitude control.

This work was done by Paul Timmerman and Virgil Shields of Caltech for NASA's Jet Propulsion Laboratory. Further information is contained in a TSP (see page 1). NPO-43055

Phase Calibration of Antenna Arrays Aimed at Spacecraft

A document describes a method of calibrating phase differences among ground antennas in an array so that the maximum-intensity direction of the far-field interference pattern of the array coincides with the direction for aiming the antennas to enable radio communication with a distant spacecraft. The method pertains to an array typically comprising between two and four 34-m (or similar size) antennas. The antennas are first calibrated pair-wise to maximize the uplink power received at a different spacecraft that is close enough for commu-

nication via a single ground antenna.

In the calibration procedure, the phase of the signal transmitted by one of the antennas is ramped through a complete cycle, thereby causing the interference pattern to sweep over this closer spacecraft and guaranteeing that, at some point during the sweep, this spacecraft is illuminated at maximum intensity. The varying received uplink power is measured by a receiver in the closer spacecraft and the measurement data are transmitted to a ground station to enable determination of the optimum phase adjustment for the direction to the closer spacecraft. This adjustment is then translated to the look direction of the distant spacecraft, which could not be reached effectively using only one antenna.

This work was done by Victor Vilnotter, Dennis Lee, Leslie Paal, Ryan Mukai, and Timothy Cornish of Caltech for NASA's Jet Propulsion Laboratory. Further information is contained in a TSP (see page 1). NPO-43647

Ring Bus Architecture for a Solid-State Recorder

A document concisely describes a ring bus architecture for a proposed solid-state recorder (SSR) that would serve as buffer of data to be transmitted from a spacecraft to Earth. This architecture would afford fault tolerance needed for reliable operation in an anticipated high-radiation environment in which traditional SSRs cannot operate reliably. Features of the architecture include one or more controller boards and multiple memory boards interconnected in a ringlike topology. The interconnections would be high-speed serial links complying with the Institute of Electrical and Electronics Engineers (IEEE) standard 1393 (which pertains to a spaceborne fiber-optic data bus).

Accordingly, each controller and memory board would be equipped with an IEEE-1393-compliant ring-bus-interface unit. The ringlike topology and the multiplicity of memory boards (and, optionally, of controller boards) would afford the redundancy needed for fault tolerance. Each board would be a fault-containment region. The IEEE 1393 links could be

routed so that the SSR would continue to function even in the event of multiple failures. This architecture would also support scalability over a wide range. In a fully redundant configuration, it could accommodate between 1 and 125 memory boards.

This work was done by W. John Walker, Edward Kopf, and Brian Cox of Caltech for NASA's Jet Propulsion Laboratory. Further information is contained in a TSP (see page 1). NPO-45132

Image Compression Algorithm Altered To Improve Stereo Ranging

A report discusses a modification of the ICER image-data-compression algorithm to increase the accuracy of ranging computations performed on compressed stereoscopic image pairs captured by cameras aboard the Mars Exploration Rovers. (ICER and variants thereof were discussed in several prior NASA Tech Briefs articles.) Like many image compressors, ICER was designed to minimize a mean-square-error measure of distortion in reconstructed images as a function of the compressed data volume. The present modification of ICER was preceded by formulation of an alternative error measure, an image-quality metric that focuses on stereoscopic-ranging quality and takes account of image-processing steps in the stereoscopic-ranging process. This metric was used in empirical evaluation of bit planes of wavelet-transform subbands that are generated in ICER.

The present modification, which is a change in a bit-plane prioritization rule in ICER, was adopted on the basis of this evaluation. This modification changes the order in which image data are encoded, such that when ICER is used for lossy compression, better stereoscopic-ranging results are obtained as a function of the compressed data volume.

This work was done by Aaron Kiely of Caltech for NASA's Jet Propulsion Laboratory. Further information is contained in a TSP (see page 1).

This software is available for commercial licensing. Please contact Karina Edmonds of the California Institute of Technology at (626) 395-2322. Refer to NPO-44647.



National Aeronautics and
Space Administration